Pathway and mechanism of tubulin folding mediated by TRiC/CCT conjugated with its ATPase cycle revealed by cryo-EM

Caixuan Liu[1,2], Mingliang Jin[1], Shutian Wang[1,2], Wenyu Han[1,2], Qiaoyu Zhao[1,2], Yifan Wang[1,2], Cong Xu[1,2], Lei Diao[3], Yue Yin[4], Chao Peng[4], Lan Bao[2,3], Yanxing Wang[1], Yao Cong[1,2]*

[1] State Key Laboratory of Molecular Biology, National Center for Protein Science Shanghai, Shanghai Institute of Biochemistry and Cell Biology, Center for Excellence in Molecular Cell Science, Chinese Academy of Sciences, Shanghai 200031, China.

[2] University of Chinese Academy of Sciences, Beijing 100049, China.

[3] State Key Laboratory of Cell Biology, Shanghai Institute of Biochemistry and Cell Biology, Center for Excellence in Molecular Cell Science, Chinese Academy of Sciences, Shanghai 200031, China.

[4] National Facility for Protein Science in Shanghai, Zhangjiang Lab, Shanghai Advanced Research Institute, CAS, Shanghai 201210, China.

*Address correspondence to Yao Cong, cong@sibcb.ac.cn

Abstract

The eukaryotic chaperonin TRiC/CCT assists the folding of about 10% of cytosolic proteins through an ATP-driven conformational cycle, and the essential cytoskeleton protein tubulin is the obligate substrate of TRiC. Here, we present an ensemble of cryo-EM structures of human TRiC throughout its ATPase cycle, with three of them revealing endogenously engaged tubulin in different folding stages. Our structural and XL-MS analyses suggested a gradual upward translocation and stabilization of tubulin within the TRiC chamber accompanying TRiC ring closure. Remarkably, in the closed TRiC-tubulin-S3 map resolved to 3.1-Å-resolution, we captured a near-natively folded tubulin. We found the near-natively folded tubulin engaging through its N and C domains mainly with the A and I domains of the CCT3/6/8 subunits through electrostatic and hydrophilic interactions, while the tubulin I domain was found to remain dynamic. Moreover, we also showed the potential role of TRiC C-terminal tails in substrate stabilization and folding. Our study delineates the pathway and molecular mechanism of TRiC-mediated tubulin folding conjugated with TRiC ATPase cycle, and may also inform the design of therapeutic agents targeting TRiC-tubulin interactions.

Introduction

Chaperonins are protein folding nanomachines that play an essential role in maintaining cellular homeostasis and are important in all kingdoms of life, and their dysfunction is closely related to cancer and neurodegenerative diseases[1-3]. Chaperonins provide a cage-like environment for proteins to fold in isolation, unimpaired by aggregation, and in some cases actively modulate the folding pathway of the encapsulated protein[4-7]. The eukaryotic group II chaperonin TRiC/CCT assists the folding of ~10% of cytosolic proteins, including the key cytoskeletal proteins actin and tubulin, cell cycle regulator CDC20, and VHL tumor suppressor[8-15]. TRiC is the most complex chaperon system identified to date. It has a double-ring structure, and each ring consists of eight paralogous subunits (namely CCT1-CCT8) arranged in a specific order[16-21]. Each TRiC subunit consists of three domains: the substrate-recognition apical domain (A domain) and the ATP-binding equatorial domain (E domain) linked by the intermediate domain (I domain). TRiC-mediated substrate folding is closely related to its ATP-driven conformational cycle[22-25]. TRiC has been proved to display subunit specificity in the complex assembly, ATP consumption and ring closure[16,19,26,27].

In the past two decades, constant efforts have been made to capture the TRiC-substrate binary complexes so as to reveal the mechanism of TRiC-assisted substrate folding for diverse substrates[7,9,11,15,28-32]. Still, there remains lacking of the atomic-resolution structural details revealing the dynamic process of TRiC-mediated substrate folding throughout its ATP-driven conformational cycle, due to the relative low binding efficiency between TRiC and the pretreated unfolded substrates (usually involving applying urea or GuHCl *in vitro*) and due to the potential conformational and compositional heterogeneity of the binary complex[33].

Tubulin, the building block of microtubule, is the *in vivo* obligate substrate of TRiC[15,34-37]. Highly conserved α- and β-tubulin heterodimers assemble into dynamic microtubules[38] , which are ubiquitous cytoskeletal polymers essential for the life of all eukaryotic cells. Microtubules are involved in a wide range of cellular functions, from

cell motility and intracellular transport to, most fundamentally, cell division[36,39-43]. Tubulin (~50 kDa) contains three domains: the GTP-binding N domain, the I domain containing the site that binds the chemotherapeutic Taxol, and the C domain responsible for interacting with microtubule-binding proteins. Previous studies reported structures of the TRiC-tubulin complex in the apo or ATP-binding state at relatively low resolution (~25 Å) or intermediate resolution (5.5 Å) determined using cryo-electron microscopy (cryo-EM) or X-ray crystallography[9,15,32]. However, a complete picture with molecular details of the TRiC-directed tubulin folding driven by ATP binding and hydrolysis remains obscure. Moreover, it has been reported that the small molecule I-Trp can disrupt constitutively associated β-tubulin/TRiC, causing severe cell apoptosis, indicating that targeting the TRiC/tubulin complex could serve as a novel chemotherapeutic strategy[44,45].

To capture the TRiC-directed tubulin folding pathway, we determined an ensemble of cryo-EM structures of human TRiC (hTRiC) throughout its ATP-driven conformational cycle. Three of these structures showed endogenously bound tubulin. Strikingly, in the closed-state TRiC-tubulin-S3 structure, we captured a near-natively folded tubulin and disclosed atomic details of the interaction between tubulin and TRiC. We also found that the C- and N-terminal tails (abbreviated as C-/N-termini) of TRiC play distinct roles in substrate stabilization/folding and TRiC allosteric coordination, respectively, with the N-terminus of CCT8 possibly contributing to tubulin folding in the opposite ring. Collectively, our study captured a thorough picture of the pathway and molecular mechanism of TRiC-mediated tubulin folding conjugated with the TRiC ATPase cycle.

Results

Cryo-EM structure of TRiC in complex with tubulin

We purified endogenous human TRiC from HEK293F cells (Extended Data Fig. 1a; hereafter, “TRiC” refers to human TRiC unless otherwise noted), which was validated by sodium dodecyl sulfate-polyacrylamide gel electrophoresis (SDS-PAGE)

93 and mass spectrometry (MS) analyses (Fig. 1a and Supplementary Table 1). The result
94 of NADH-coupled enzymatic assay further validated the ATPase activity of the
95 purified TRiC (Extended Data Fig. 1b). Moreover, our SDS-PAGE analysis also
96 indicated the presence of an extra associated protein at ~50 kDa (Fig. 1a), which was
97 suggested to be mainly β-tubulin (TUBB5) by the MS analysis (Supplementary Table
98 1). The PSM value from the MS analysis, indicating the relative abundance of a
99 certain protein[46], showed the abundance of β-tubulin was comparable to that of
100 individual TRiC subunit. The existence of tubulin was further confirmed by native
101 electrophoresis combined with western blot and chemical cross-linking-coupled mass
102 spectrometry (XL-MS) analysis (Fig. 1b-c, Supplementary Table 2). Our XL-MS
103 analysis detected five cross-links between tubulin and CCT3/4/6/8 subunits (Fig. 1c).
104 Taken together, these data indicated a co-existence of TRiC with tubulin.

105 We then performed cryo-EM study on the endogenously purified TRiC sample
106 (Extended Data Fig. 1c). Two cryo-EM maps, including an open state TRiC with an
107 empty chamber, and another TRiC map also in the open conformation but displaying
108 an extra density in one chamber, were determined at 3.1- and 4.1-Å-resolution,
109 respectively (Fig. 1d-g, and Extended Data Fig. 2). Interestingly, although we
110 performed buffer exchange multiple times to remove remaining nucleotide in the final
111 stage of purification, CCT3/6/8 subunits appeared to have bound nucleotide density in
112 both maps (Extended Data Fig. 3e-f), which were suggested to be ADP according to
113 an ADP/ATP ratio assay (Extended Data Fig. 3g), in line with our previous report on
114 the yeast TRiC system[19]. Accordingly, these two open TRiC maps are also in the
115 "nucleotide partially preloaded" (NPP) state. We then denoted the free open TRiC
116 map as TRiC-NPP. The NPP state is equivalent to the "apo" state in typical
117 conformational cycle studies of ATPase chaperonins[24,47,48], mimicking the starting
118 point in the conformational cycle of the chaperonin itself.

119 Our TRiC-NPP map showed a conformation overall similar to that of the
120 available substrate-free human TRiC cryo-EM map also in the open state at 7.7-Å-
121 resolution, with determined subunit assignment[49]. We then fit the TRiC-NPP map to

their map (Extended Data Fig. 4a), both displaying the following characteristic features known for open-state TRiC: (1) CCT1 being the most outward tilted subunit, a feature common for yeast, bovine, and human TRiCs[16,19,7,49]; (2) the A domain of CCT2 being quite disordered (Fig. 1d), also observed in open bovine TRiC[7,24]; (3) each ring displaying a tetramer-of-dimer pattern as in the open bovine TRiC[24]; (4) the largest gap existing between CCT1 and CCT4[50] (Extended Data Fig. 4b). These features allowed us to assign the subunits for the TRiC-NPP map. We then built an atomic model for TRiC-NPP (Extended Data Fig. 3a-d). Further inspection of the TRiC-NPP structure revealed the characteristic V476-K484 insertion in the E domain of CCT1 (Extended Data Fig. 4c-d), corroborating our subunit assignment for this map.

Moreover, our TRiC-NPP map showed a chunk of density between the two equators blocking the two chambers (Fig. 1e), with this density symmetrically contacting the N-/C-terminal extensions of CCT5/7 and CCT5'/7' from both rings of TRiC (Extended Data Fig. 4e). Hence, we assigned the density as the unstructured N- and C-terminal tails of TRiC subunits, also observed in the available human and bovine TRiC open-state maps[7,49] (Extended Data Fig. 4f-g). Moreover, the A/I domains of CCT2 hemisphere subunits (including CCT4/2/5/7)[21,28] appeared less well resolved as in the bovine and human open-state TRiC structures[7,24,28,49], indicating an intrinsic dynamic nature in these regions. Indeed, our 3D variability analysis (3DVA) using cryoSPARC[51] suggested the A/I domains of CCT1/4/2/5/7 to be overall relatively dynamic—and strikingly, with those of CCT7/5/1 showing continuous outward/inward tilting motions of up to ~23°/6°/5°, respectively (Extended Data Fig. 4h and Supplementary Video 1).

Importantly, for the other map derived from the same dataset (38.4% of the population, Fig. 1f-g and Extended Data Fig. 2a), we attributed the captured extra density in the cis-ring chamber to the trapped β-tubulin co-purified with TRiC, based on our biochemical and MS data (Fig. 1a-c, Extended Data Fig. 4i and Supplementary Table 1-2). We denoted this map as TRiC-tubulin-S1, which was also in the NPP state

151 with the consecutive CCT3/6/8 subunits loaded with nucleotides in both rings
152 (Extended Data Fig. 3f). This demonstrated that TRiC can engage with substrate in
153 the nucleotide partially loaded NPP state. A previous crystal structure of bovine TRiC
154 with bound tubulin also revealed two nucleotides per-ring in non-consecutive
155 subunits[15]. The TRiC conformation in the S1 map was observed to resemble that of
156 our TRiC-NPP structure (Extended Data Fig. 4j), we then followed the same subunit
157 assignment. Overall, the substrate density appeared to associate with the E domain of
158 every TRiC subunit, mainly with the C-terminus and stem loop of these subunits (Fig.
159 1h). The bovine TRiC-tubulin crystal structure also revealed that the tubulin forms
160 contact with the stem loops of three TRiC subunits[15].

161 **Tubulin translocation within TRiC chamber accompanying TRiC**
162 **conformational cycle**

163 To further capture the TRiC-directed tubulin folding process conjugated with
164 TRiC ATPase cycle, we performed cryo-EM study on TRiC in the presence of 1 mM
165 ATP-AlFx (Extended Data Fig. 1d), an ATP-hydrolysis-transition state analog that can
166 trigger TRiC ring closure[22,23,25]. In the resulting dataset, the majority (65.4%) of the
167 particles were in the closed conformation and resolved to a resolution of 2.9 Å, while
168 the remaining (34.6%) particles were in the open conformation and resolved to a
169 resolution of 4.2 Å (Fig. 2a and Extended Data Fig. 5a-c). In the open state, obvious
170 substrate density was observed in the cis-ring, and we denoted this map as TRiC-
171 tubulin-S2. For the closed state, through focused classification in the chamber region,
172 we obtained two maps: one map at a resolution of 3.1 Å showed tubulin density in the
173 cis-ring chamber (termed TRiC-tubulin-S3), and the other map at a resolution of 3.2
174 Å showed no substrate in the chamber, but a central tail density in an orientation
175 different from that in the open state (denoted as TRiC-ADP-AlFx, discussed below)
176 (Fig. 2c-g, Extended Data Fig. 5a-b, d-f). Moreover, we performed XL-MS analysis
177 on the ATP-AlFx presented TRiC sample, and detected 17 cross-links between tubulin
178 and TRiC subunits (Fig. 2h and Supplementary Table 3), further substantiating the
179 notion that the captured substrate was indeed tubulin.

The overall TRiC conformation of the open-state S2 map was observed to be similar to that of the TRiC-NPP map (Extended Data Fig. 5g). We then followed the subunit assignments of TRiC-NPP to assign those of S2. For the closed-state S3 map, a characteristic kink feature in the CCT6 α-helical protrusion H8 and the unique insertions in CCT1/4/6 were clearly visualized (Extended Data Fig. 6), facilitating the subunit assignment in the maps of the closed TRiC with similar features. We then built an atomic model for each of the S2, S3 and TRiC-ADP-AlFx maps (Extended Data Fig. 7a-f). We found that for these three structures, all subunits from both rings bound nucleotides (Extended Data Fig. 7g-i). For the S2 map, the nucleotide density was fitted well by the ATP structure (Extended Data Fig. 7j), indicating S2 was in the ATP-binding state. For the closed S3 and TRiC-ADP-AlFx structures, with their E-domain local resolution reached ~2.8 to 2.9 Å (Extended Data Fig.5d-e), the nucleotide densities for all subunits matched ADP-AlFx and a magnesium ion very well, in addition to a water molecule attacking the γ-phosphate of nucleotide, involved in the formation of the ATP hydrolysis reaction center (Fig. 2i and Extended Data Fig. 7k). These features suggested the two closed-state maps were in the ATP hydrolysis transition state.

Indeed, the CCT2 subunit in the S2 map appeared less dynamic and better resolved than that in the NPP-state S1 map (Figs. 1d, f and Fig. 2a), indicating CCT2 may have been stabilized after ATP binding. Accordingly, the substrate density in the S2 map appeared larger than that in the S1 map, with this difference attributed to ATP-binding-induced stabilization of TRiC (Fig. 1h and Fig. 2j). Notably, in TRiC-tubulin-S2, the substrate density was found to be closely associated with all the three domains of CCT6/8 and to form loose contacts with the E domains of the other subunits (Fig. 2j) as well as with the central tail region (Fig. 2b). Compared with TRiC-tubulin-S1, it appears that ATP-binding could drive tubulin to translocate from the E domains of all the subunits slightly up towards the A/I domains, to converge more on the CCT6/8 subunits, while nevertheless remaining bound to all of the E domains (Fig. 2j).

209 **ATP-driven TRiC ring closure is the determinant step for tubulin folding**

210 Importantly, inspection of our TRiC-tubulin-S3 map revealed a well resolved
211 tubulin density in one chamber of TRiC hanging underneath its dome predominantly
212 on the CCT6 hemisphere subunits (including CCT1/3/6/8)[21,28] (Fig. 2d-e and Fig. 3a-
213 b). The tubulin density appeared to resemble the conformation of native tubulin (Fig.
214 3b), and hence we defined the captured tubulin as being in the near-natively folded
215 state. Overall, the N and C domains of tubulin were relatively well resolved with
216 atomic details observed (Fig. 3c). While the majority of the I domain of tubulin was
217 captured (Fig. 3b), a small portion (sequence: 242-249, 279-283, 319-348) facing the
218 central chamber was less well resolved (Fig. 3a, d), implying an intrinsically dynamic
219 nature for this region. Interestingly, this dynamic region was noted to overlap with its
220 interaction interface with α-tubulin to form a tubulin heterodimer or with cofactor A
221 for the release of tubulin[43,52] (Fig. 3d), indicating this intrinsically dynamic region of
222 the tubulin I domain may only be stabilized by engaging with these factors.
223 Substantiating this speculation, our XL-MS analysis showed that tubulin I domain
224 Lys252 forms crosslinks with all subunits of TRiC with the cross-linked Cα-Cα
225 distances ranging from 20 to 61 Å (Fig. 3e), indicating a highly dynamic structure in
226 this region. These results were also in line with a recent report showing reovirus σ3
227 capsid protein acting as a dynamic substrate within the TRiC chamber[28]. Note that this
228 Lys252 had been shown to play an essential role in interacting with the γ-phosphate of
229 the GTP in the α-tubulin portion of the tubulin dimer[43] (Fig. 3f). Collectively, our data
230 suggested that the I domain region of β-tubulin is intrinsically dynamic since it is
231 "born" before associating with α-tubulin to form the tubulin dimer.

232 Inspection of the S3 map showed that tubulin engages with TRiC mainly through
233 its N/C domains, forming intimate salt-bridge- and H-bond-mediated contacts with all
234 three domains of the CCT6 hemisphere subunits (Fig. 3g, h and Supplementary Table
235 4). The tubulin I domain also loosely interacts with CCT2 hemisphere subunits
236 through association with the A-domain protrusion loop and C-termini of CCT7/5/2/4
237 (Fig. 3g). Indeed, tubulin showed an obviously larger interaction area with the CCT6

238 hemisphere subunits than with the CCT2 hemisphere ones (Extended Data Fig. 7l).
239 Furthermore, inspection of S3 structure also unprecedently revealed the protrusion
240 loop, loop^{H10}, loop^{H9}, C-terminus, and stem loop to be the main structural elements of
241 TRiC involved in its interaction with tubulin (Fig. 3g-h and Extended Data Fig. 7m-n).
242 Our TRiC-tubulin-S3 structure appeared overall comparable with a recent structure of
243 closed TRiC-tubulin complex[53], in terms of tubulin orientation and binding location
244 within TRiC chamber.

245 In addition, our XL-MS data suggested that before adding nucleotide, tubulin
246 only crossed linked with the E domains of TRiC; while in the presence of ATP-AlFx,
247 additional XLs formed with the A/I domains of TRiC (Fig. 3i), indicating an upward
248 shift of tubulin induced by ATP binding and hydrolysis. Indeed, more TRiC A and I
249 domain regions were observed to be involved in the interaction with tubulin in the S2
250 and S3 states (Figs. 2j and 3g) than in the S1 state (Fig. 1h). Inspection of the S2 and
251 S3 maps suggested that ATP-hydrolysis could induce considerable downward rotation
252 of the A and E domains of TRiC from the open to closed state (Extended Data Fig. 7o).
253 These substantial movements could dramatically reduce the chamber volume, and
254 hence restrain the conformational landscape of the substrate and lead to a more
255 stabilized substrate through intimate interactions with the TRiC A/I domains. In the
256 meanwhile, the mechanical force generated from TRiC ring closure could provide
257 extra energy to help the substrate overcome the energy barrier and transform towards
258 the global energy minimum. This may be a general mechanism for TRiC-mediated
259 substrate folding.

260 **Tubulin engages with closed TRiC through both electrostatic and hydrophilic**
261 **interactions**

262 We then inspected the closed TRiC-tubulin-S3 structure to derive the interaction
263 properties between tubulin and TRiC. Here the electrostatic surface property inside
264 the TRiC chamber was observed to be asymmetric, with the CCT6 hemisphere more
265 positively charged and the CCT2 hemisphere relatively negatively charged (Fig. 4a-b),
266 in line with previous reports on yeast and bovine TRiC[21]. Interestingly, the engaged

267 tubulin N/C domains appear negatively charged, complementary with the contacting
268 CCT6 hemisphere (Fig. 4b). This observation was also consistent with our findings
269 that numerous salt bridges formed between TRiC CCT6 hemisphere subunits and
270 tubulin N/C domains (Fig. 3h). The electrostatic surface of the tubulin I domain was
271 found to be not complementary with the related region of TRiC (Fig. 4a-b), consistent
272 with the lack of a strong interaction between them (Fig. 3g, Extended Data Fig. 7l).
273 Taken together, our S3 structure revealed previously unreported strong electrostatic
274 interactions between the tubulin N/C domains and the TRiC CCT6 hemisphere
275 subunits.

276 Inspection of the S3 structure also suggested an enrichment of hydrophilic
277 residues at the interaction interfaces between the TRiC inner dome and tubulin,
278 creating a mostly polar TRiC-tubulin interface in the closed chamber (Fig. 4c). This
279 type of polar interface was also seen in the TRiC-σ3 complex[30]. Taken together, our
280 data suggested that the closed-state TRiC interacts with its obligate substrate tubulin
281 through a combination of electrostatic and hydrophilic interactions to stabilize this
282 substrate and facilitate its folding.

283 We have previously showed that yeast TRiC can close both rings in the presence
284 of natural nucleotide ATP[16]. Here we performed further cryo-EM study on human
285 TRiC incubated with ATP at 1 mM, a physiological concentration of ATP in the
286 cell[16,54], and obtained two maps, including an open-state TRiC and a both-ring-closed
287 TRiC (27.2 % of the population) (Extended Data Fig. 8a-c). The closed TRiC map
288 showed that all nucleotide pockets were occupied, in addition to a tubulin density
289 within one TRiC chamber in a position and orientation similar to that observed in the
290 TRiC-tubulin-S3 map (Extended Data Fig. 8d-e). Collectively, these results suggested
291 that the double-closed state for both yeast and human TRiC indeed exists in the
292 presence of natural nucleotide, in line with a recent *in situ* cryo-ET study on neuron
293 cells[55].

294 **Cryo-EM map of TRiC-ADP**

295 To capture the complete TRiC ATPase cycle, we determined a cryo-EM map of

296 TRiC in the presence of ADP to a resolution of 3.3 Å (termed TRiC-ADP, Fig. 5a-b,
297 Extended Data Fig. 1e, 9, and 10a-b). In this map, TRiC is in the open conformation,
298 overall similar to that of TRiC-NPP (Extended Data Fig. 10c), but with all of the
299 subunits loaded with ADP (Fig. 5c, Extended Data Fig. 10d). However, other than the
300 remaining unstructured tail density, there was no engaged tubulin anymore within
301 TRiC chamber (Fig. 5b). Corroborate to this, our XL-MS data showed no detected
302 cross-links between TRiC and tubulin after the ADP incubation (Fig. 5d), indicating
303 that under our experimental condition ADP binding on TRiC could potentially
304 contribute to a release of tubulin from TRiC regardless of tubulin folding status. We
305 performed further 3DVA on the dataset and found TRiC-ADP to be very dynamic,
306 with all the subunits (including the most stable CCT6) displaying outward/inward
307 tilting motions (Extended Data Fig. 10e, Supplementary Video 2). We then postulate
308 that the dynamic nature of TRiC-ADP may contribute to the substrate release in this
309 state. Still, we should mention that here we used the TRiC-ADP structure to mimic the
310 state that, after releasing γ-phosphate, TRiC reached the open state and then also
311 released the substrate.

312 **The C- and N-termini of TRiC play distinct roles in substrate folding and TRiC**
313 **allosteric coordination**

314 Here, we showed that in each of the four open-state TRiC structures (TRiC-NPP,
315 S1, S2, and TRiC-ADP), there is a central unstructured tail density between the two
316 equators (Fig. 1e, g, Fig. 2b and Fig. 5b). Moreover, in both the S1 and S2 structures,
317 the resolved portions of the TRiC C-termini and the extended unstructured tail density
318 apparently form contacts with the tubulin substrate and hence potentially stabilize the
319 substrate (Fig. 1g-h and Fig. 2b, j).

320 Strikingly, in the closed TRiC-tubulin-S3 structure, the N-terminus of almost all
321 of the TRiC subunits were stabilized and very well resolved (Extended Data Fig. 11).
322 Specifically, the N-termini of all subunits except CCT4 were observed to contact H1
323 of the neighboring subunit, and those of CCT2/4/5/7/8 to involve in the inter-ring
324 allosteric network (Extended Data Fig. 11a-g). This observation is consistent with our

325 previous finding in yeast TRiC, suggesting that the extra layer of N-terminal allosteric
326 network could play important roles in TRiC ring closure[16]. Intriguingly, we observed
327 the N-terminus of CCT8' from the trans-ring adopting a bent conformation and
328 extending all the way to the cis-ring to associate with the tubulin N domain (Fig. 4d),
329 in addition to being involved in the inter-ring allosteric network by linking the
330 CCT6/6' N-termini and CCT3 stem loop together. This indicated that CCT8 may play
331 a critical role in substrate stabilization/folding besides being involved in TRiC inter-
332 ring cooperativity.

333 Notably, in the closed S3 state, we also resolved a portion of the C-terminal
334 extensions for most TRiC subunits (except CCT4), and captured the uncharacterized
335 direct interactions between these C-terminal extensions of TRiC and tubulin (Fig. 4e).
336 These C-terminal extensions, mostly hydrophilic (Fig. 4f), stretch out from the
337 surrounding subunits towards the center of TRiC chamber to form physical contacts
338 with tubulin, and hence appearing like a net holding and stabilizing tubulin within the
339 TRiC chamber (Fig. 4e), which may facilitate tubulin folding. Consistent with this,
340 previous studies suggested that the C-termini of GroEL form contacts with its
341 substrate, which could enhance and accelerate substrate folding, and that the
342 hydrophilic residues on the C-termini are critical for substrate folding[56-59].

343 Discussion

344 Tubulin is the building block of the microtubule, which is critical to many cellular
345 processes, and the eukaryotic chaperonin TRiC is required for tubulin biogenesis.
346 Here, we captured snapshots of tubulin folding pathway mediated by TRiC, by
347 acquiring six cryo-EM structures of human TRiC in its ATPase cycle with three of
348 them engaged with endogenous tubulin in different folding stages (Fig. 1, 2, and 5).
349 Importantly, our TRiC-tubulin-S3 structure revealed a near-natively folded tubulin
350 engaged with closed TRiC in one chamber, primarily with the A/I domains of the
351 CCT3/6/8 subunits through electrostatic and hydrophilic interactions (Fig. 4a-c). We
352 also noticed the interaction of TRiC termini with tubulin in the open TRiC-tubulin-S1

353 and -S2 states (Fig. 1h, 2j), and found that in the closed S3 state the N terminus of
354 CCT8 from the opposite ring and the C-terminal extensions of almost all TRiC
355 subunits may play a role in tubulin stabilization and folding (Fig. 4d-f).

356 **Proposed pathway and mechanism of TRiC-mediated tubulin folding**

357 Here we propose a complete picture of TRiC-mediated tubulin folding pathway
358 and mechanism conjugated with the ATP-driven conformational cycle of TRiC (Fig.
359 6a). After being translated from ribosomes, nascent tubulin polypeptides are delivered
360 to TRiC by co-chaperon prefoldin to enter its folding pathway associated with the
361 TRiC ATPase cycle[49,60]. Subsequently, tubulin can be released inside TRiC chamber,
362 making contacts with the E domains of all of the TRiC subunits and with the
363 unstructured termini of TRiC, to form the TRiC-tubulin-S1 state, in which the tubulin
364 is relatively dynamic (step 1). After ATP binds to TRiC, with the resulting
365 stabilization of the folding machinery, tubulin can be gradually translocated upwards
366 to associate with the A/I domains of CCT6/8 in addition to keeping contacts with the
367 E domains of all of the subunits (step 2). Once hydrolysis of ATP triggers TRiC ring
368 closure (with the involvement of TRiC N-termini), C-terminal extensions of TRiC and
369 the N-terminus of CCT8 from the opposite ring could stabilize and potentially
370 facilitate the upward translocation of tubulin to result in the formation of intimate
371 electrostatic and hydrophilic interactions between the A domain of CCT6 hemisphere
372 subunits and the N/C domains of tubulin. These directional contacts and constraints
373 on the tubulin N/C domains could facilitate its folding towards the native state, and
374 the mechanical force generated by TRiC ring closure including the considerable
375 downward rotation of the A domain of every TRiC subunit could be propagated to
376 tubulin and drive it to overcome the energy barrier to transform towards the global
377 minimum reaching the folded state-(step 3). Subsequently, in the γ-phosphate released
378 open TRiC-ADP state, the associated tubulin could be released from TRiC chamber
379 (step 4). Based on previous reports, the dynamic β-tubulin I domain could then be
380 recognized and capped by cofactor A, followed by the assembly of β-tubulin with α-
381 tubulin into tubulin heterodimers with the assistance of cofactors C, D, and E[61-63].

382 Finally, the tubulin heterodimers assemble into the microtubule, which goes on to
383 perform its biological functions.

384 **Conformational landscape of TRiC-mediated tubulin folding**

385 Without TRiC-assisted folding, nascent tubulins are prone to form aggregates due
386 to the high energy barrier for spontaneous folding to reach the native folded state[64]. In
387 the current work, by capturing multiple intermediate states of tubulin folding assisted
388 by TRiC, we were able to derive a hypothetical energy landscape of the three distinct
389 states of TRiC-tubulin on the basis of nucleotide binding status, complex stability, and
390 population distribution (Fig. 6b). In TRiC-tubulin-S1, the engagement with TRiC
391 could potentially stabilize the nascent tubulin, leading it to overcome the first energy
392 barrier to reach a lower level in the energy landscape. Still, the tubulin at this stage
393 remains quite dynamic, accompanying the dynamic nature of TRiC in the NPP state
394 with only CCT3/6/8 subunits preloaded with ADP (Extended Data Fig. 3f-g). The
395 subsequent binding of ATP to all of the TRiC subunits could drive TRiC and
396 associated tubulin to overcome the next barrier and to stabilize in the steadier TRiC-
397 tubulin-S2 state, evidenced by the observation that the engaged tubulin density here
398 becoming further stabilized and appearing larger. Only when ATP-hydrolysis provides
399 sufficient chemical energy to enable TRiC to overcome the final energy barrier,
400 shutting both rings and becoming transformed to the most stable TRiC-tubulin-S3
401 state, the confined tubulin is now folded to its near native state inside the closed TRiC
402 chamber. This step may be the rate-limiting step in tubulin folding process. Thus, the
403 ATP-mediated gradual stabilization of TRiC guides tubulin along a pathway that
404 avoids deep kinetic traps in the folding energy landscape. That is to say, binding of
405 tubulin to TRiC could lower the folding energy barrier of tubulin and result in its
406 stabilization, so that it eventually reaches its folded state accompanying ATP-driven
407 TRiC ring closure.

408 **Asymmetric working mechanism of TRiC**

409 TRiC subunits have been previously demonstrated to display a gradient of ATP
410 affinities[27], as well as differences in nucleotide binding[15,19,28] and consumption[16], with

411 these features closely related to the structural asymmetry among TRiC subunits[19,24,65].
412 In the current study, our results further depicted that in the TRiC-NPP state, the bound
413 ADP in CCT3/6/8 may play a role in stabilizing these subunits, making them appear
414 less intrinsically dynamic than the other subunits (Fig. 1d, f). Consequently, CCT3/6/8
415 may serve as a dock for an initial engagement of tubulin (Fig. 1h and Fig. 2j), and
416 eventually for close electrostatic and hydrophilic contacts with the N/C domains of
417 tubulin in its nearly folded state (Fig. 3h and Fig. 4a-c). Consistently, previous studies
418 also suggested important roles of CCT3/6/8 in the recognition of other substrates such
419 as mLST8, reovirus σ3 capsid protein, and AML1-175[26-28]. Taken together, the
420 asymmetry of TRiC subunits in structural features and nucleotide consumption may
421 contribute to TRiC-assisted substrate folding.

422 In addition, we found that along with the substrate folding, from a relatively
423 disordered state to an ordered state, TRiC also appears to follow a similar trend:
424 transforming from the relatively dynamic and asymmetric open S1 state to the
425 stabilized, rather symmetrical both-ring-closed S3 state. And during this process, the
426 nucleotide occupancy status also appears to change, from an initial partial occupancy
427 in the NPP state to the full occupancy in all the subunits of TRiC, with the nucleotide
428 states becoming more homologous (Extended Data Fig. 3f, 7g-h). In the nucleotide
429 binding and consumption, as well as ring closure, the asymmetric machinery—TRiC
430 displays a stepwise mechanism[16,19] rather than a concerted manner as in the Group I
431 system[66,67]. As has been suggested previously[68], the asymmetry or non-concerted
432 nature of TRiC in the open state could be beneficial for its ability to recognize and
433 engage with diverse substrates. Moreover, despite that our study and most other
434 studies revealed only one substrate engaged with TRiC[7,11,28,29,69,70], there was a crystal
435 structure showing that TRiC can simultaneously bind two tubulins, one per ring[15],
436 implying two substrates could interact with a TRiC complex simultaneously at least
437 under certain physiological conditions[68] and both rings of TRiC may have the ability
438 to perform substrate folding concurrently for efficient protein quality control under
439 these conditions.

440 In summary, our study depicted a thorough picture of the pathway and
441 conformational landscape of TRiC-mediated tubulin folding accompanying the
442 ATPase cycle of the folding machinery. Furthermore, our determination of the
443 interaction sites between tubulin and the closed TRiC chamber is beneficial for the
444 development of novel and effective therapeutic agents specifically targeting TRiC-
445 tubulin interactions.

446 ## Methods

447 **Purification of human TRiC**. Human TRiC was purified from HEK293F cells
448 according to the published protocol with some modifications[28,49,71]. Briefly, the pellet
449 was lysed with iced MQA-10% glycerol buffer (50 mM NaCl, 20 mM Hepes pH 7.4,
450 5 mM $MgCl_2$, 1 mM DTT, 10% glycerol, 1 mM PMSF, and 2 mM ATP) using one
451 Protease Inhibitor Cocktail Tablet (Roche) per 100 mL of the lysate. The lysed
452 material was then subjected to centrifugation (20,000 g for 30 min to remove cellular
453 debris and nuclei and then 140,000 g for 1.5 h to remove the ribosome) in order to
454 separate the cytoplasmic fraction. The resulting supernatant was filtered using a 0.44
455 μm filter membrane, and then passed through a Q Sepharose column (GE Healthcare).
456 TRiC was eluted in a gradient from 40 to 80% MQB-5% glycerol (MQA with 1 M
457 NaCl). The fractions containing TRiC were pooled, diluted with MQA to ensure an
458 NaCl concentration of about 100 mM, and applied to a Heparin HiTrap HP column
459 (GE Healthcare). TRiC was eluted in a gradient from 20 to 65% MQB-5% glycerol.
460 The fractions containing TRiC were pooled and incubated with 10 mM ATP on a
461 shaker (220 rpm, 37 °C，30 min) to allow TRiC to cycle and release substrate before
462 performing gel filtration chromatography (GFC). The sample was then concentrated
463 down to 0.5 mL and loaded onto a Superose 6 Increase 10/300 GL column (GE
464 Healthcare) with MQA-5% glycerol without ATP. TRiC eluted at about 13-15.5 mL of
465 the size-exclusion column, consistent with that of a 1-MDa complex. Finally, the
466 sample was subjected multiple times to buffer exchange to remove remaining ATP in
467 the buffer, and we obtained biologically active TRiC (Extended Data Fig. 1a-b).

468 It is noteworthy that TRiC-mediated folding of tubulin is associated with release
469 of predominantly nonnative forms of tubulin from chaperonin, and with the majority
470 of released tubulin requiring further rounds of binding/release to reach its native
471 state[72]. This indicates the released nonnative substrate could re-bind on TRiC to go
472 through further round of ATPase cycle. In our experimental condition, it is possible
473 that the tubulin in TRiC-tubulin-S1 has already gone through one or several ATPase
474 cycles.

475 **ATPase activity assay**. The ATP hydrolysis rate of TRiC was measured by
476 performing an NADH-coupled assay[73]. In this assay, each ATP hydrolysis event
477 allows for a conversion of one molecule of phosphoenolpyruvate into pyruvate
478 catalyzed by pyruvate kinase, with pyruvate then converted to lactate by L-lactate
479 dehydrogenase, which results in oxidation of a single NADH molecule. Loss of
480 NADH over time, a measure quantifiably proportional to the ATP hydrolysis rate, was
481 monitored in the current work by measuring the decrease in absorbance of light at a
482 wavelength of 340 nm. All of the assays were conducted at room temperature in a
483 buffer containing 10 mM HEPES/NaOH pH 7.5, 50 mM NaCl, and 10 mM $MgCl_2$, in
484 the presence of 1 mM ATP. Experiments were performed in triplicate using 0.3 μM of
485 the protein complex. Absorbance was measured in a 200 μl reaction volume using a
486 96-well plate reader. Data analysis was performed using Graph Pad Prism 8.

487 **ADP/ATP ratio assay.** To identify the form of the nucleotide in our purified human
488 TRiC, we carried out luciferin-luciferase reactions with an ADP/ATP ratio assay kit[74]
489 (Sigma-Aldrich). To release the bound nucleotide from TRiC for measurement, the
490 TRiC sample was first digested with proteinase K, according to a previously
491 published protocol[75] with minor modifications. TRiC proteolytic-digestion
492 experiments were carried out by adding a 1 μl aliquot of 2 mg/ml proteinase K to a 19
493 μl aliquot of 4.5 mg/ml TRiC in dilution buffer (20 mM Hepes-KOH pH 7.4, 50 mM
494 NaCl, 5 mM $MgCl_2$, 1 mM DTT, and 5% glycerol). The digestion was performed at
495 37 °C for 1 h. The reactions were then terminated by adding PMSF (to a final
496 concentration of 5 mM) into the reaction mixture and waiting for 10 minutes.
497 Afterwards, the nucleotide form in the TRiC sample was identified by using the
498 ADP/ATP ratio assay kit according to the manufacturer's protocol, and the RLU
499 values of ATP and ADP were measured with a Synergy Neo2 multimode reader
500 (BioTek).

501 **Cross-linking and mass spectrometry analysis**. The purified TRiC was cross-linked
502 by using bis[sulfosuccinimidyl] suberate (BS^3) (Sigma), with a spacer arm of 11.4 Å
503 between their Cα carbons, on ice for 2 hours. The final concentration of the

504 crosslinker was 2 mM. The reaction was then terminated by using 50 mM Tris-HCl
505 pH 7.5 at room temperature for 15 minutes. For the sample containing ATP-AlFx, the
506 purified TRiC was incubated with 1 mM ATP, 5 mM $MgCl_2$, 5 mM $Al(NO_3)_3$, and 30
507 mM NaF for 1 h at 37 °C, and the resulting product was cross-linked by using BS^3
508 following the above-mentioned conditions. Cross-linked complexes were precipitated
509 and digested for 16 hours at 37 °C by using trypsin at an enzyme-to-substrate ratio of
510 1:50 (w/w). The tryptic-digested peptides were desalted and loaded on an in-house
511 packed capillary reverse-phase C18 column (length of 40 cm, 100 µm ID x 360 µm
512 OD, 1.9 µm particle size, pore diameter of 120 Å) connected to an Easy LC 1200
513 system. The samples were analyzed with a 120 min-HPLC gradient of 6% to 35% of
514 buffer B (buffer A: 0.1% formic acid in Water; buffer B: 0.1% formic acid in 80%
515 acetonitrile) at 300 nL/minute. The eluted peptides were ionized and directly
516 introduced into a Q-Exactive mass spectrometer using a nano-spray source. Survey
517 full-scan MS spectra (from m/z 300–1800) were acquired using an Orbitrap analyzer
518 with a resolution r=70,000 at an m/z of 400. Cross-linked peptides were identified and
519 evaluated using pLink2 software[76].

520 **Cryo-EM sample preparation.** To prepare the vitrified sample of TRiC, the purified
521 TRiC was diluted to 1.2 mg/ml, and an aliquot of 2 µl of this sample was applied onto
522 a plasma cleaned holey carbon grid (Quantifoil, R1.2/1.3, 200 mesh). The grid was
523 blotted with Vitrobot Mark IV (Thermo Fisher Scientific) and then plunged into liquid
524 ethane cooled by liquid nitrogen. To prepare the sample of TRiC in the presence of 1
525 mM ATP-AlFx, the purified TRiC was diluted to 1.2 mg/ml, and incubated with 1
526 mM ATP, 5 mM $MgCl_2$, 5 mM Al $(NO_3)_3$, and 30 mM NaF at 37 °C for 1 h prior to
527 freezing. To prepare the sample of TRiC with 1 mM ADP, the purified TRiC was
528 diluted to 1.2 mg/ml, and incubated with 1 mM ADP and 5 mM $MgCl_2$ at 37 °C for 1
529 h prior to freezing. Moreover, to prepare the sample of TRiC in the presence of 1 mM
530 ATP, the purified TRiC was diluted to 1.2 mg/ml, and incubated with 1 mM ATP and
531 5 mM $MgCl_2$ at 37 °C for 30 s before freezing. We then followed the above-
532 mentioned procedure to prepare the vitrified sample in each case.

533 **Data acquisition**. For each of the experimental sample conditions mentioned above
534 except for TRiC-ATP dataset, cryo-EM movies of the sample were collected using a
535 Titan Krios electron microscope (Thermo Fisher Scientific) operated at an
536 accelerating voltage of 300 kV with a nominal magnification of 18,000x (yielding a
537 pixel size of 1.318 Å, Table 1). The movies were recorded on a K2 Summit direct
538 electron detector (Gatan) operated in the super-resolution mode under low-dose
539 condition in an automatic manner using SerialEM[77]. The exposure time for each
540 frame was 0.2 s and the total accumulation time was 7.6 s, leading to a total
541 accumulated dose of 38 $e^-/Å^2$ on the specimen. For TRiC-ATP dataset, the movies
542 were collected in a magnification of 81,000x (yielding a pixel size of 0.89 Å, Table 1)
543 utilizing a K3 direct electron detector (Gatan) operated in the counting mode under a
544 low-dose condition in an automatic manner using EPU (Thermo Fisher Scientific).
545 Each frame was exposed for 0.05 s, and the total accumulation time was 2 s, leading
546 to a total accumulated dose of 50 $e^-/Å^2$ on the specimen.

547 **Image processing and 3D reconstruction.** We performed single-particle analysis
548 mainly using Relion 3.1[78,79] unless otherwise specified (Table 1). All images were
549 aligned and summed using MotionCor2[80]. After CTF parameter determination using
550 CTFFIND4[81], particle auto-picking, manual particle checking, and reference-free 2D
551 classification, particles with TRiC features were remained for further processing.

552 For the TRiC sample before addition of nucleotides, 761,665 particles were
553 picked from the original micrographs, and after 2D classification, 709,192 particles
554 remained (Extended Data Fig. 2a). These particles were subjected to 3D refinement,
555 and then were re-extracted and re-centered using the refinement coordinates. After
556 one round of no-align 3D classification and another round of 3D classification, we
557 then combined the substrate-containing particles (including class 1 from the first
558 round and class 3 from the second round) together, and performed another round of
559 3D classification, generating a substrate-containing class with 169,098 particles. After
560 carrying out CTF refinement and polishing on these particles, we obtained a map with
561 weak substrate density at 4.0-Å-resolution. We subtracted the substrate density and

562 performed a no-align 3D classification, and a good class with 68.4% of the particles
563 were reverted to the original particles. We then performed a local refinement on these
564 particles and reconstructed a 4.1-Å-resolution TRiC-tubulin-S1 map displaying better
565 substrate density. For the substrate-free class 4 particles from the second round of 3D
566 classification, we performed another round of 3D classification, resulting in a better
567 class having 185,216 particles. After CTF refinement and Bayesian polishing, these
568 particles were refined to a 3.1-Å-resolution TRiC-NPP map. The resolution estimation
569 was based on the gold-standard Fourier Shell Correlation (FSC) criterion of 0.143.

570 For the dataset of TRiC in the presence of ATP-AlFx, after 2D classification,
571 544,809 particles remained (Extended Data Fig. 5a). These particles were subjected to
572 3D classification. The particles from class 4, displaying closed-state features, were
573 subjected to another round of 3D classification and a resulting better class with
574 168,472 particles was further refined to produce a 2.9-Å-resolution map with weak
575 substrate density inside the TRiC chamber. Thus, we focused on the extra density
576 inside the chamber and performed a no-align 3D classification, generating 4 classes.
577 Particles from classes 1 and 2, appearing to have tubulin density, were combined
578 (total of 103,406 particles) and refined to produce a 3.1-Å-resolution TRiC-tubulin-S3
579 map; class 3 (62,412 particles), having an extra tail density, were used to reconstruct a
580 3.2-Å-resolution TRiC-ADP-AlFx map. In addition, particles of classes 1-3 from the
581 first round of 3D classification were subjected to another round of 3D classification
582 and yielded a better class with 98,046 particles that were refined to produce a 4.3-Å-
583 resolution map. Through focused refinement and focused classification, we eventually
584 obtained a 4.2-Å-resolution map with tubulin density in one ring, termed TRiC-
585 tubulin-S2.

586 For the dataset of TRiC-ADP, after 2D classification, 344,486 and 319,306
587 particles remained for dataset 1 and 2, respectively (Extended Data Fig. 9a). After
588 refinement and re-centering, the particles were further cleaned in cryoSPARC through
589 2D classification and heterogeneous refinement. Then the good particles were
590 subjected to two rounds of 3D classification in Relion 3.1. Subsequently, the better-

591 resolved classes 3/4 from dataset 1 and classes 2/3 from dataset 2 were combined and
592 subjected to one more round of 3D classification. The better class with 239,315
593 particles were further refined to a 3.3-Å-resolution TRiC-ADP map.

594 For the TRiC-ATP dataset, after 2D classification 225,085 particles remained
595 (Extended Data Fig. 8a). These particles were refined and re-extracted, and further
596 cleaned up in cryoSPARC by 2D classification and heterogeneous refinement to yield
597 three classes. Class 1 open-state particles were subjected to another round of
598 heterogeneous refinement, and the 111,413 particles of the better class 1 were refined
599 to produce a 3.8-Å-resolution TRiC-ATP-open map. Closed-state particles from class
600 2 of the first round of heterogeneous refinement were subjected to another round of
601 heterogeneous refinement, and particles from the better class 2 were refined in Relion
602 3.1 to produce a 4.5-Å-resolution TRiC-ATP-closed map.

603 **Model building by flexible fitting**. We built the homology models for human TRiC
604 in the open and closed states and for tubulin (TUBB5) using the SWISS-MODEL
605 server[82], with the cryo-EM structures of the yeast TRiC in the open and closed
606 conformations (PDB ID: 5GW4, 5GW5, 6KS6[16,19]) and the cryo-EM structure of
607 human TUBB3 tubulin (PDB ID: 5JCO[83]) as templates, respectively. Afterwards, we
608 refined the model against the corresponding cryo-EM map using Rossetta[84], and then
609 Phenix[85]. Furthermore, to improve the fitting between model and map, we performed
610 real-space refinement using COOT[86]. Finally, we used Phenix again for the last round
611 of flexible fitting of the entire complex.

612 We used UCSF Chimera and ChimeraX for generating figures and performing
613 electrostatic surface property calculations[87,88]. Interaction surface analysis was
614 conducted by using the PISA server[89].

Acknowledgements

We are grateful to the staffs of the NCPSS Electron Microscopy facility, Database and Computing facility, Mass Spectrometry facility, and Protein Expression and Purification facility for instrumental support and technical assistance. This work was supported by grants from the Strategic Priority Research Program of CAS (XDB37040103), the National Basic Research Program of China (2017YFA0503503), the NSFC (32130056, 31670754 and 31872714), the Shanghai Academic Research Leader (20XD1404200), Shanghai Pilot Program for Basic Research–CAS, Shanghai Branch (JCYJ-SHFY-2022-008), and the CAS Facility-based Open Research Program.

Author contributions

Y.C. and C.L. designed the experiments. C.L. purified the proteins and performed functional analysis with the involvement of Q.Z.. C.L. and M.J. with the involvement of S.W. and W.H. collected the cryo-EM data. C.L. with the involvement of C.X. and Y-F. Wang performed data reconstruction and model building. Y-X. Wang, L.D., and L.B. helped supervise the functional analysis. C.P., C.L., and Y.Y. performed the XL-MS analysis. Y.C. and C.L. analyzed the structure and wrote the manuscript.

Data availability

All data presented in this study are available within the figures and in the Supplementary Information. Cryo-EM maps and the associated models have been deposited in the EMDB and Protein Data Bank, respectively, with the accession ID as the following: TRiC-NPP (EMDB-32922, PDB-7X0A), TRiC-tubulin-S1 (EMDB-32903, PDB-7WZ3), TRiC-tubulin-S2 (EMDB-32989, PDB-7X3J), TRiC-tubulin-S3 (EMDB-32923, PDB-7X0S), TRiC-ADP-AlFx (EMDB-32926, PDB-7X0V), TRiC-ADP (EMDB-32993, PDB-7X3U), TRiC-ATP-closed (EMDB-33025, PDB-7X6Q), TRiC-ATP-open (EMDB-33053, PDB-7X7Y).

Competing interests

641 The authors declare no competing interests.

Reference

1 Tam, S. *et al.* The chaperonin TRiC blocks a huntingtin sequence element that promotes the conformational switch to aggregation. *Nature Structural & Molecular Biology* **16**, 1279-U1298, doi:10.1038/nsmb.1700 (2009).

2 Khabirova, E. *et al.* The TRiC/CCT chaperone is implicated in Alzheimer's disease based on patient GWAS and an RNAi screen in Abeta-expressing Caenorhabditis elegans. *PLoS One* **9**, e102985, doi:10.1371/journal.pone.0102985 (2014).

3 Pereira, J. H. *et al.* Mechanism of nucleotide sensing in group II chaperonins. *EMBO J* **31**, 731-740, doi:10.1038/emboj.2011.468 (2012).

4 Hayer-Hartl, M., Bracher, A. & Hartl, F. U. The GroEL-GroES Chaperonin Machine: A Nano-Cage for Protein Folding. (2016).

5 Balchin, D., Hayer-Hartl, M. & Hartl, F. U. In vivo aspects of protein folding and quality control. *Science* **353**, aac4354, doi:10.1126/science.aac4354 (2016).

6 Joachimiak, L. A., Walzthoeni, T., Liu, C. W., Aebersold, R. & Frydman, J. The structural basis of substrate recognition by the eukaryotic chaperonin TRiC/CCT. *Cell* **159**, 1042-1055, doi:10.1016/j.cell.2014.10.042 (2014).

7 Balchin, D., Milicic, G., Strauss, M., Hayer-Hartl, M. & Hartl, F. U. Pathway of Actin Folding Directed by the Eukaryotic Chaperonin TRiC. *Cell* **174**, 1507-1521 e1516, doi:10.1016/j.cell.2018.07.006 (2018).

8 Llorca, O. *et al.* Eukaryotic type II chaperonin CCT interacts with actin through specific subunits. *Nature* **402**, 693-696, doi:Doi 10.1038/45294 (1999).

9 Llorca, O. *et al.* Eukaryotic chaperonin CCT stabilizes actin and tubulin folding intermediates in open quasi-native conformations. *Embo Journal* **19**, 5971-5979, doi:DOI 10.1093/emboj/19.22.5971 (2000).

10 Camasses, A., Bogdanova A Fau - Shevchenko, A., Shevchenko A Fau - Zachariae, W. & Zachariae, W. The CCT chaperonin promotes activation of the anaphase-promoting complex through the generation of functional Cdc20. (2003).

11 Plimpton, R. L. *et al.* Structures of the Gbeta-CCT and PhLP1-Gbeta-CCT complexes reveal a mechanism for G-protein beta-subunit folding and Gbetagamma dimer assembly. *Proc Natl Acad Sci U S A* **112**, 2413-2418, doi:10.1073/pnas.1419595112 (2015).

12 Kasembeli, M. *et al.* Modulation of STAT3 folding and function by TRiC/CCT chaperonin. *PLoS Biol* **12**, e1001844, doi:10.1371/journal.pbio.1001844 (2014).

13 Trinidad, A. G. *et al.* Interaction of p53 with the CCT complex promotes protein folding and wild-type p53 activity. *Mol Cell* **50**, 805-817, doi:10.1016/j.molcel.2013.05.002 (2013).

14 McClellan, A. J., Scott Md Fau - Frydman, J. & Frydman, J. Folding and quality control of the VHL tumor suppressor proceed through distinct chaperone pathways. (2005).

15 Munoz, I. G. *et al.* Crystal structure of the open conformation of the mammalian chaperonin CCT in complex with tubulin. *Nat Struct Mol Biol* **18**, 14-19, doi:10.1038/nsmb.1971 (2011).

16 Jin, M. *et al.* An ensemble of cryo-EM structures of TRiC reveal its conformational landscape and subunit specificity. *Proc Natl Acad Sci U S A* **116**, 19513-19522, doi:10.1073/pnas.1903976116 (2019).

17 Kalisman, N., Adams, C. M. & Levitt, M. Subunit order of eukaryotic TRiC/CCT chaperonin by cross-linking, mass spectrometry, and combinatorial homology modeling. *Proc Natl Acad Sci*

U S A **109**, 2884-2889, doi:10.1073/pnas.1119472109 (2012).

18 Wang, H., Han, W., Takagi, J. & Cong, Y. Yeast Inner-Subunit PA–NZ-1 Labeling Strategy for Accurate Subunit Identification in a Macromolecular Complex through Cryo-EM Analysis. *Journal of Molecular Biology* **430**, 1417-1425, doi:https://doi.org/10.1016/j.jmb.2018.03.026 (2018).

19 Zang, Y. *et al.* Staggered ATP binding mechanism of eukaryotic chaperonin TRiC (CCT) revealed through high-resolution cryo-EM. *Nat Struct Mol Biol* **23**, 1083-1091, doi:10.1038/nsmb.3309 (2016).

20 Zang, Y. *et al.* Development of a yeast internal-subunit eGFP labeling strategy and its application in subunit identification in eukaryotic group II chaperonin TRiC/CCT. *Sci Rep* **8**, 2374, doi:10.1038/s41598-017-18962-y (2018).

21 Leitner, A. *et al.* The molecular architecture of the eukaryotic chaperonin TRiC/CCT. *Structure* **20**, 814-825, doi:10.1016/j.str.2012.03.007 (2012).

22 Booth, C. R. *et al.* Mechanism of lid closure in the eukaryotic chaperonin TRiC/CCT. *Nat Struct Mol Biol* **15**, 746-753, doi:10.1038/nsmb.1436 (2008).

23 Cong, Y. *et al.* 4.0-A resolution cryo-EM structure of the mammalian chaperonin TRiC/CCT reveals its unique subunit arrangement. *Proc Natl Acad Sci U S A* **107**, 4967-4972, doi:10.1073/pnas.0913774107 (2010).

24 Cong, Y. *et al.* Symmetry-free cryo-EM structures of the chaperonin TRiC along its ATPase-driven conformational cycle. *EMBO J* **31**, 720-730, doi:10.1038/emboj.2011.366 (2012).

25 Meyer, A. S. *et al.* Closing the folding chamber of the eukaryotic chaperonin requires the transition state of ATP hydrolysis. *Cell* **113**, 369-381, doi:10.1016/s0092-8674(03)00307-6 (2003).

26 Liu, C. *et al.* Cryo-EM study on the homo-oligomeric ring formation of yeast TRiC/CCT subunits reveals TRiC ring assembly mechanism. *BioRxiv*, doi:10.1101/2021.02.24.432666 (2021).

27 Reissmann, S. *et al.* A gradient of ATP affinities generates an asymmetric power stroke driving the chaperonin TRIC/CCT folding cycle. *Cell Rep* **2**, 866-877, doi:10.1016/j.celrep.2012.08.036 (2012).

28 Cuellar, J. *et al.* Structural and functional analysis of the role of the chaperonin CCT in mTOR complex assembly. *Nat Commun* **10**, 2865, doi:10.1038/s41467-019-10781-1 (2019).

29 Roh, S. H., Kasembeli, M. M., Galaz-Montoya, J. G., Chiu, W. & Tweardy, D. J. Chaperonin TRiC/CCT Recognizes Fusion Oncoprotein AML1-ETO through Subunit-Specific Interactions. *Biophys J* **110**, 2377-2385, doi:10.1016/j.bpj.2016.04.045 (2016).

30 Knowlton, J. J. *et al.* Structural and functional dissection of reovirus capsid folding and assembly by the prefoldin-TRiC/CCT chaperone network. *Proceedings of the National Academy of Sciences* **118**, e2018127118, doi:10.1073/pnas.2018127118 (2021).

31 Llorca, O. *et al.* Analysis of the interaction between the eukaryotic chaperonin CCT and its substrates actin and tubulin. *J Struct Biol* **135**, 205-218, doi:10.1006/jsbi.2001.4359 (2001).

32 Llorca, O. *et al.* The 'sequential allosteric ring' mechanism in the eukaryotic chaperonin-assisted folding of actin and tubulin. *EMBO J* **20**, 4065-4075, doi:10.1093/emboj/20.15.4065 (2001).

33 Jin, M., Liu, C., Han, W. & Cong, Y. in *Macromolecular Protein Complexes II: Structure and Function* (eds J. Robin Harris & Jon Marles-Wright) 625-654 (Springer International

729 Publishing, 2019).
730 34 Leroux, M. R. & Hartl, F. U. Protein folding: Versatility of the cytosolic chaperonin TRIC/CCT.
731 *Current Biology* **10**, R260-R264, doi:Doi 10.1016/S0960-9822(00)00432-2 (2000).
732 35 Ursic, D. & Culbertson, M. R. The Yeast Homolog to Mouse Tcp-1 Affects Microtubule-
733 Mediated Processes. *Molecular and Cellular Biology* **11**, 2629-2640, doi:Doi
734 10.1128/Mcb.11.5.2629 (1991).
735 36 Yaffe, M. B. *et al.* TCP1 complex is a molecular chaperone in tubulin biogenesis. *Nature* **358**,
736 245-248, doi:10.1038/358245a0 (1992).
737 37 Sternlicht, H. *et al.* The t-complex polypeptide 1 complex is a chaperonin for tubulin and actin
738 in vivo. *Proceedings of the National Academy of Sciences of the United States of America* **90**,
739 9422-9426, doi:10.1073/pnas.90.20.9422 (1993).
740 38 Sullivan, K. F. Structure and Utilization of Tubulin Isotypes. *Annual Review of Cell Biology* **4**,
741 687-716, doi:10.1146/annurev.cb.04.110188.003351 (1988).
742 39 Breuss, M. *et al.* Mutations in the β-tubulin gene TUBB5 cause microcephaly with structural
743 brain abnormalities. *Cell reports* **2**, 1554-1562, doi:10.1016/j.celrep.2012.11.017 (2012).
744 40 Poirier, K. *et al.* Mutations in the neuronal β-tubulin subunit TUBB3 result in malformation of
745 cortical development and neuronal migration defects. *Human Molecular Genetics* **19**, 4462-
746 4473, doi:10.1093/hmg/ddq377 (2010).
747 41 Tischfield, M. A. *et al.* Human TUBB3 Mutations Perturb Microtubule Dynamics, Kinesin
748 Interactions, and Axon Guidance. *Cell* **140**, 74-87, doi:10.1016/j.cell.2009.12.011 (2010).
749 42 Ballatore, C., Lee, V. M. & Trojanowski, J. Q. Tau-mediated neurodegeneration in Alzheimer's
750 disease and related disorders. *Nat Rev Neurosci* **8**, 663-672, doi:10.1038/nrn2194 (2007).
751 43 Nogales, E. & Alushin, G. M. Tubulin and Microtubule Structure: Mechanistic Insights Into
752 Dynamic Instability and Its Biological Relevance doi:10.1016/b978-0-12-809633-8.08056-0
753 (2017).
754 44 Lin, Y. F., Tsai, W. P., Liu, H. G. & Liang, P. H. Intracellular beta-tubulin/chaperonin containing
755 TCP1-beta complex serves as a novel chemotherapeutic target against drug-resistant tumors.
756 *Cancer Res* **69**, 6879-6888, doi:10.1158/0008-5472.CAN-08-4700 (2009).
757 45 Liu, Y. J., Kumar, V., Lin, Y. F. & Liang, P. H. Disrupting CCT-beta : beta-tubulin selectively kills
758 CCT-beta overexpressed cancer cells through MAPKs activation. *Cell Death Dis* **8**, e3052,
759 doi:10.1038/cddis.2017.425 (2017).
760 46 Chen, J. *et al.* Cryo-EM of mammalian PA28alphabeta-iCP immunoproteasome reveals a
761 distinct mechanism of proteasome activation by PA28alphabeta. *Nat Commun* **12**, 739,
762 doi:10.1038/s41467-021-21028-3 (2021).
763 47 Chaudhry, C., Horwich, A. L., Brunger, A. T. & Adams, P. D. Exploring the structural dynamics
764 of the E.coli chaperonin GroEL using translation-libration-screw crystallographic refinement
765 of intermediate states. *J Mol Biol* **342**, 229-245, doi:10.1016/j.jmb.2004.07.015 (2004).
766 48 Clare, D. K. *et al.* ATP-triggered conformational changes delineate substrate-binding and -
767 folding mechanics of the GroEL chaperonin. *Cell* **149**, 113-123, doi:10.1016/j.cell.2012.02.047
768 (2012).
769 49 Gestaut, D. *et al.* The Chaperonin TRiC/CCT Associates with Prefoldin through a Conserved
770 Electrostatic Interface Essential for Cellular Proteostasis. *Cell* **177**, 751-765 e715,
771 doi:10.1016/j.cell.2019.03.012 (2019).
772 50 Cuellar, J. *et al.* The Molecular Chaperone CCT Sequesters Gelsolin and Protects it from

773 Cleavage by Caspase-3. *J Mol Biol* **434**, 167399, doi:10.1016/j.jmb.2021.167399 (2021).
774 51 Punjani, A. & Fleet, D. J. 3D variability analysis: Resolving continuous flexibility and discrete
775 heterogeneity from single particle cryo-EM. *J Struct Biol* **213**, 107702,
776 doi:10.1016/j.jsb.2021.107702 (2021).
777 52 You, L., Gillilan, R. & Huffaker, T. C. Model for the yeast cofactor A-beta-tubulin complex
778 based on computational docking and mutagensis. *Journal of Molecular Biology* **341**, 1343-
779 1354, doi:10.1016/j.jmb.2004.06.081 (2004).
780 53 Kelly, J. J. *et al.* Snapshots of actin and tubulin folding inside the TRiC chaperonin. *Nat Struct*
781 *Mol Biol*, doi:10.1038/s41594-022-00755-1 (2022).
782 54 Huang, H. B. *et al.* Physiological levels of ATP negatively regulate proteasome function. *Cell*
783 *Research* **20**, 1372-1385, doi:10.1038/cr.2010.123 (2010).
784 55 Guo, Q. *et al.* In Situ Structure of Neuronal C9orf72 Poly-GA Aggregates Reveals Proteasome
785 Recruitment. *Cell* **172**, 696-705 e612, doi:10.1016/j.cell.2017.12.030 (2018).
786 56 Machida, K., Kono-Okada, A., Hongo, K., Mizobata, T. & Kawata, Y. Hydrophilic residues 526
787 KNDAAD 531 in the flexible C-terminal region of the chaperonin GroEL are critical for
788 substrate protein folding within the central cavity. *J Biol Chem* **283**, 6886-6896,
789 doi:10.1074/jbc.M708002200 (2008).
790 57 Ishino, S. *et al.* Effects of C-terminal Truncation of Chaperonin GroEL on the Yield of In-cage
791 Folding of the Green Fluorescent Protein. *J Biol Chem* **290**, 15042-15051,
792 doi:10.1074/jbc.M114.633636 (2015).
793 58 Chen, D. H. *et al.* Visualizing GroEL/ES in the act of encapsulating a folding protein. *Cell* **153**,
794 1354-1365, doi:10.1016/j.cell.2013.04.052 (2013).
795 59 Weaver, J. *et al.* GroEL actively stimulates folding of the endogenous substrate protein PepQ.
796 *Nat Commun* **8**, 15934, doi:10.1038/ncomms15934 (2017).
797 60 Hansen, W. J., Cowan, N. J. & Welch, W. J. Prefoldin-nascent chain complexes in the folding of
798 cytoskeletal proteins. *Journal of Cell Biology* **145**, 265-277, doi:DOI 10.1083/jcb.145.2.265
799 (1999).
800 61 Gao, Y., Vainberg, I. E., Chow, R. L. & Cowan, N. J. Two cofactors and cytoplasmic chaperonin
801 are required for the folding of alpha- and beta-tubulin. *Mol Cell Biol* **13**, 2478-2485,
802 doi:10.1128/mcb.13.4.2478-2485.1993 (1993).
803 62 Grynberg, M., Jaroszewski, L. & Godzik, A. Domain analysis of the tubulin cofactor system: a
804 model for tubulin folding and dimerization. *BMC Bioinformatics* **4**, 46, doi:10.1186/1471-
805 2105-4-46 (2003).
806 63 Tian, G. *et al.* Pathway Leading to Correctly Folded β-Tubulin. *Cell* **86**, 287-296,
807 doi:10.1016/S0092-8674(00)80100-2 (1996).
808 64 Hartl, F. U., Bracher, A. & Hayer-Hartl, M. Molecular chaperones in protein folding and
809 proteostasis. *Nature* **475**, 324-332, doi:10.1038/nature10317 (2011).
810 65 Rivenzon-Segal, D., Wolf, S. G., Shimon, L., Willison, K. R. & Horovitz, A. Sequential ATP-
811 induced allosteric transitions of the cytoplasmic chaperonin containing TCP-1 revealed by EM
812 analysis. *Nat Struct Mol Biol* **12**, 233-237, doi:10.1038/nsmb901 (2005).
813 66 Ma, J. P., Sigler, P. B., Xu, Z. H. & Karplus, M. A dynamic model for the allosteric mechanism of
814 GroEL. *Journal of Molecular Biology* **302**, 303-313, doi:10.1006/jmbi.2000.4014 (2000).
815 67 Horovitz, A. & Willison, K. R. Allosteric regulation of chaperonins. *Curr Opin Struc Biol* **15**, 646-
816 651, doi:10.1016/j.sbi.2005.10.001 (2005).

817 68 Yebenes, H., Mesa, P., Munoz, I. G., Montoya, G. & Valpuesta, J. M. Chaperonins: two rings for
818 folding. *Trends Biochem Sci* **36**, 424-432, doi:10.1016/j.tibs.2011.05.003 (2011).
819 69 Dekker, C. *et al.* The crystal structure of yeast CCT reveals intrinsic asymmetry of eukaryotic
820 cytosolic chaperonins. *EMBO J* **30**, 3078-3090, doi:10.1038/emboj.2011.208 (2011).
821 70 Knowlton, J. J. *et al.* Structural and functional dissection of reovirus capsid folding and
822 assembly by the prefoldin-TRiC/CCT chaperone network. *Proc Natl Acad Sci U S A* **118**,
823 doi:10.1073/pnas.2018127118 (2021).
824 71 Knee, K. M., Sergeeva, O. A. & King, J. A. Human TRiC complex purified from HeLa cells
825 contains all eight CCT subunits and is active in vitro. *Cell Stress Chaperones* **18**, 137-144,
826 doi:10.1007/s12192-012-0357-z (2013).
827 72 Farr, G. W., Scharl, E. C., Schumacher, R. J., Sondek, S. & Horwich, A. L. Chaperonin-mediated
828 folding in the eukaryotic cytosol proceeds through rounds of release of native and nonnative
829 forms. *Cell* **89**, 927-937, doi:10.1016/s0092-8674(00)80278-0 (1997).
830 73 Norby, J. G. Coupled Assay of Na+,K+-Atpase Activity. *Method Enzymol* **156**, 116-119 (1988).
831 74 Polletta, L. *et al.* SIRT5 regulation of ammonia-induced autophagy and mitophagy. *Autophagy*
832 **11**, 253-270, doi:10.1080/15548627.2015.1009778 (2015).
833 75 Szpikowska, B. K., Swiderek Km Fau - Sherman, M. A., Sherman Ma Fau - Mas, M. T. & Mas, M.
834 T. MgATP binding to the nucleotide-binding domains of the eukaryotic cytoplasmic
835 chaperonin induces conformational changes in the putative substrate-binding domains.
836 (1998).
837 76 Lu, S. *et al.* Mapping native disulfide bonds at a proteome scale. *Nature Methods* **12**, 329-
838 U373, doi:10.1038/Nmeth.3283 (2015).
839 77 Mastronarde, D. N. Automated electron microscope tomography using robust prediction of
840 specimen movements. *Journal of Structural Biology* **152**, 36-51,
841 doi:10.1016/j.jsb.2005.07.007 (2005).
842 78 Scheres, S. H. W. Semi-automated selection of cryo-EM particles in RELION-1.3. *Journal of*
843 *structural biology* **189**, 114-122, doi:10.1016/j.jsb.2014.11.010 (2015).
844 79 Fernandez-Leiro, R. & Scheres, S. H. W. A pipeline approach to single-particle processing in
845 RELION. *Acta Crystallographica Section D-Structural Biology* **73**, 496-502,
846 doi:10.1107/S2059798316019276 (2017).
847 80 Zheng, S. Q. *et al.* MotionCor2: anisotropic correction of beam-induced motion for improved
848 cryo-electron microscopy. *Nature methods* **14**, 331-332, doi:10.1038/nmeth.4193 (2017).
849 81 Rohou, A. & Grigorieff, N. CTFFIND4: Fast and accurate defocus estimation from electron
850 micrographs. *J Struct Biol* **192**, 216-221, doi:10.1016/j.jsb.2015.08.008 (2015).
851 82 Arnold, K., Bordoli, L., Kopp, J. & Schwede, T. The SWISS-MODEL workspace: a web-based
852 environment for protein structure homology modelling. *Bioinformatics* **22**, 195-201,
853 doi:10.1093/bioinformatics/bti770 (2006).
854 83 Vemu, A. *et al.* Structure and Dynamics of Single-isoform Recombinant Neuronal Human
855 Tubulin. *Journal of Biological Chemistry* **291**, 12907-12915, doi:10.1074/jbc.C116.731133
856 (2016).
857 84 DiMaio, F. *et al.* Atomic-accuracy models from 4.5-A cryo-electron microscopy data with
858 density-guided iterative local refinement. *Nature methods* **12**, 361-365,
859 doi:10.1038/nmeth.3286 (2015).
860 85 Adams, P. D. *et al.* PHENIX: a comprehensive Python-based system for macromolecular

861 structure solution. *Acta Crystallogr D* **66**, 213-221, doi:10.1107/S0907444909052925 (2010).
862 86 Emsley, P. & Cowtan, K. Coot: model-building tools for molecular graphics. *Acta*
863 *Crystallographica Section D-Biological Crystallography* **60**, 2126-2132,
864 doi:10.1107/S0907444904019158 (2004).
865 87 Pettersen, E. F. *et al.* UCSF chimera - A visualization system for exploratory research and
866 analysis. *J Comput Chem* **25**, 1605-1612, doi:10.1002/jcc.20084 (2004).
867 88 Goddard, T. D. *et al.* UCSF ChimeraX: Meeting modern challenges in visualization and analysis.
868 *Protein Science* **27**, 14-25, doi:10.1002/pro.3235 (2018).
869 89 Schlee, S. *et al.* Prediction of quaternary structure by analysis of hot spot residues in protein-
870 protein interfaces: the case of anthranilate phosphoribosyltransferases. *Proteins* **87**, 815-825,
871 doi:10.1002/prot.25744 (2019).

872

873 **FIGURES**

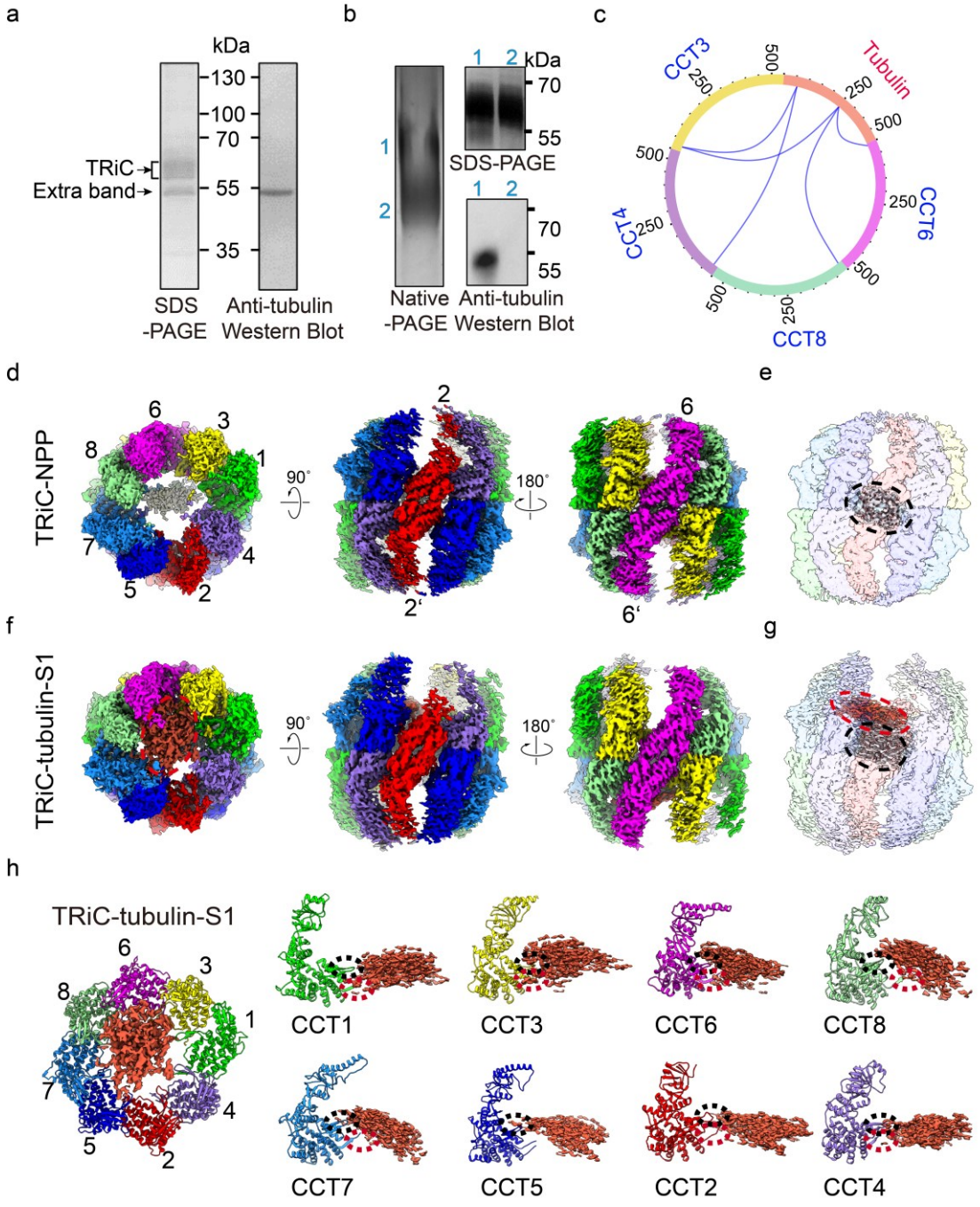

874

875 **Fig. 1 | Cryo-EM structures of the endogenously purified TRiC with associated**
876 **tubulin. a**, Sodium dodecyl sulfate-polyacrylamide gel electrophoresis (SDS-PAGE)
877 of the endogenous human TRiC purified from HEK293F cells. This gel suggested the
878 presence of an extra associated protein at ~50 kDa, which was proved to be tubulin by
879 Western blot. **b**, Native gel analysis of TRiC, showing two bands, labeled as 1 and 2,
880 which were excised and loaded into SDS-PAGE. SDS-PAGE analysis suggested that
881 both bands contain TRiC oligomer, and there is an additional band in lane 1, which

882 contained tubulin, as shown by Western blot. **c**, XL-MS analysis of the endogenously
883 purified TRiC with associated tubulin. Identified cross-linked TRiC-tubulin contacts
884 are shown as blue lines. **d,** End-on and side views of TRiC-NPP, with the different
885 subunits in different colors and labeled. This subunit color scheme is followed in
886 subsequent figures. **e,** The unstructured N- and C-terminal tail density (in grey,
887 indicated by a black dashed ellipsoid) of TRiC subunits located between the two
888 equators in TRiC-NPP (transparent density). **f-g,** Cryo-EM map of TRiC-tubulin-S1
889 (**f**), revealing extra density (shown in red and indicated by a red dashed ellipsoid)
890 within the cis-ring chamber of TRiC (**g**). **h**, Overall binding location of tubulin (red
891 density) in the cis-ring of TRiC-tubulin-S1 (colored ribbon) (left), and the association
892 of tubulin with the E domain of every TRiC subunit, including the C-terminus
893 (indicated by dotted red ellipsoid) and stem loop (dotted black ellipsoid) (right panels).

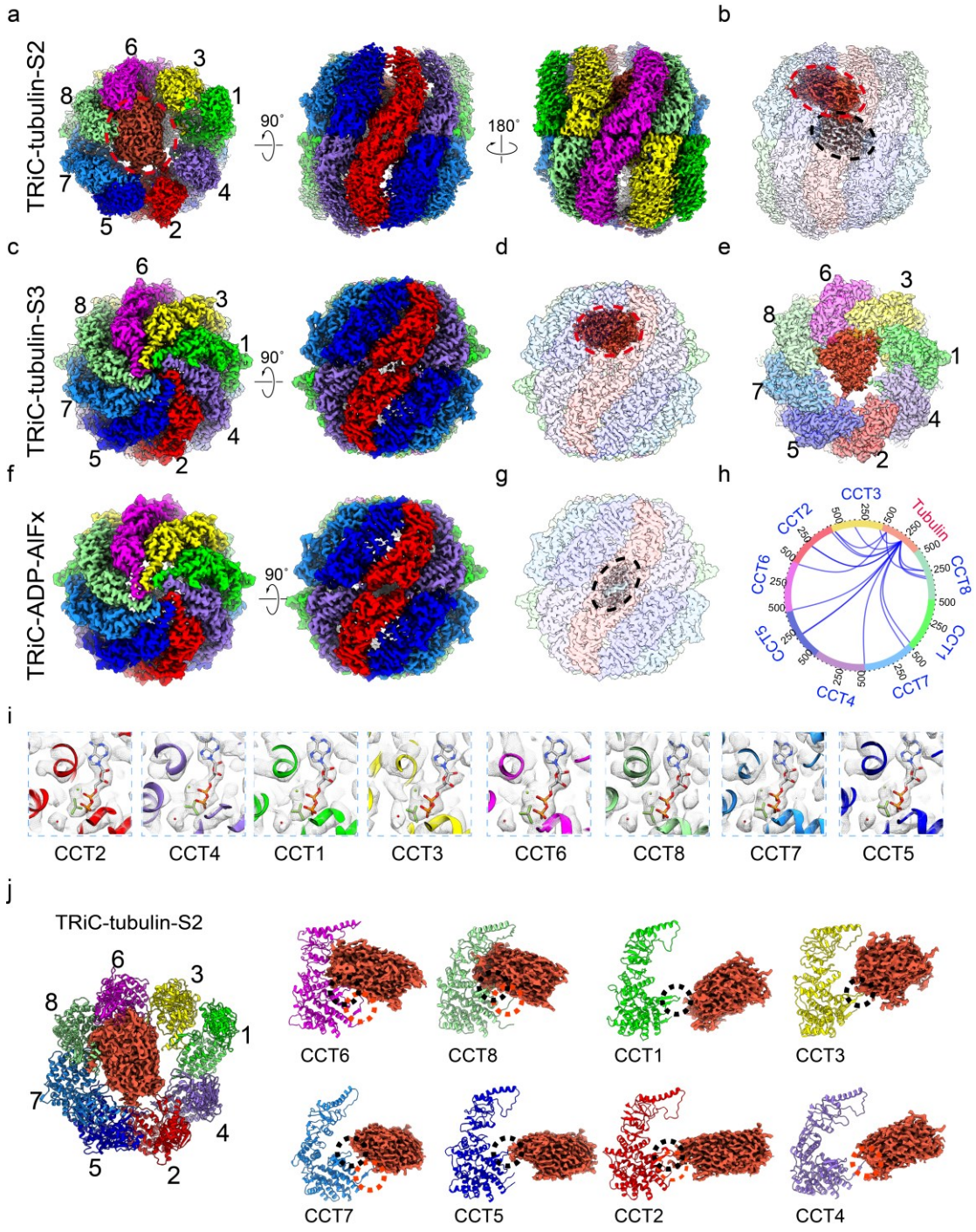

Fig. 2 | Cryo-EM structures of TRiC-tubulin in the presence of ATP-AlFx. **a-b,** Cryo-EM map of TRiC-tubulin-S2 in the open ATP-binding state (**a**), revealing a tail density (in grey) between the two equators and a tubulin density (in red) in the cis-ring of TRiC (transparent density) (**b**). The tail density contacts the tubulin density. **c-d,** Cryo-EM map of TRiC-tubulin-S3 in the closed ATP-hydrolysis transition state (**c**), revealing tubulin density in the cis-ring chamber of TRiC (**d**). **e**, Top view of the TRiC-tubulin-S3 map with TRiC A domains omitted for easier visualization, showing

902 the bound tubulin density, and indicating tubulin mainly associate with CCT6
903 hemisphere subunits (CCT1/3/6/8). **f-g,** Cryo-EM map of TRiC-ADP-AlFx (**f**),
904 revealing a C-termini mass (black dashed ellipsoid) (**g**), related to Extended Data Fig.
905 5f. **h**, XL-MS analysis of TRiC with endogenously associated tubulin in the presence
906 of ATP-AlFx. **i**, Portions of the TRiC-tubulin-S3 map in the nucleotide pocket region.
907 All of the subunits bound with ADP-AlFx (stick model) and a magnesium ion (green
908 ball), as well as a water molecule (red ball) in an attacking position, suggesting that
909 all eight subunits are in the ATP-hydrolysis transition state. **j**, Overall binding of
910 tubulin (red density) in the cis-ring of the open TRiC-tubulin-S2. Tubulin was
911 observed to contact all three domains of CCT6/8 and loosely contact the E domains,
912 including the C terminus (dotted red ellipsoid) and stem loop (dotted black ellipsoid),
913 of the remaining subunits.

914

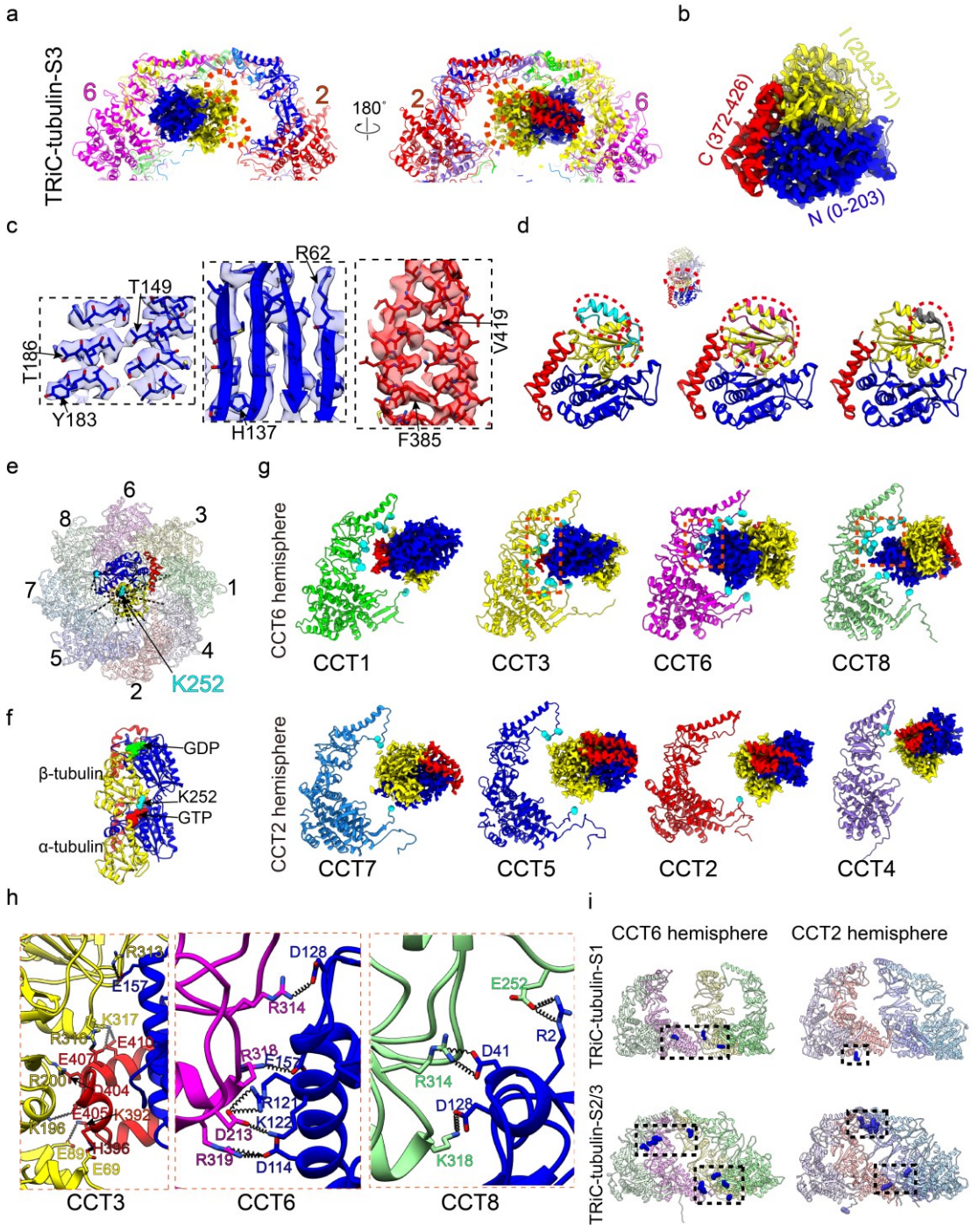

Fig. 3 | TRiC-tubulin-S3 structure showing a near-natively folded tubulin attached to the cis-ring of TRiC. **a**, Enlarged views of the engaged tubulin within the TRiC chamber in the S3 state. The tubulin N/I/C domains are rendered in blue, yellow and red, respectively, which color scheme was followed throughout. Red dotted circles indicate dynamic regions of the I domain of tubulin. **b-c**, The resolved β-tubulin inside the cis-ring of TRiC-tubulin-S3 (**b**), and its high-resolution structural features (**c**). **d**, Ribbon diagram depictions showing the unresolved dynamic portion of

923 the tubulin I domain (in cyan, left) overlapping with its interaction interface with α-
924 tubulin (in violet red, a distance cutoff of 4 Å, middle) or the interaction site with
925 cofactor A (in gray, right)[52]. **e**, Mapping of the detected XLs made by tubulin K58 and
926 K252 (cyan spheres) with the TRiC subunits in the cis-ring of TRiC-tubulin-S3. Note
927 that every TRiC subunit made at least one such XL. **f**, Ribbon diagram illustrating the
928 αβ-tubulin dimer structure, with β-tubulin facing upwards. K252 in β-tubulin and
929 bound nucleotides are shown as spheres. **g**, Ribbon diagram depictions of the
930 association between each TRiC subunit and tubulin in S3, showing the close
931 associations of the N/C domains of tubulin with CCT6 hemisphere subunits
932 CCT1/3/6/8, and loose associations of the tubulin I domain with CCT2 hemisphere
933 subunits CCT7/5/2/4. Cα atoms of the TRiC amino acid residues within 4 Å distance
934 with tubulin are shown as cyan balls. **h**, Magnified views of the regions indicated with
935 red dotted frames in **g** to show the salt bridge interactions formed between tubulin and
936 the CCT3/6/8 subunits. **i**, XL-MS-analysis-derived sites on TRiC (blue spheres)
937 crosslinked with tubulin and mapped onto the corresponding indicated TRiC structure.
938 This analysis suggested a shift in the interaction locations induced by ATP
939 binding/hydrolysis.

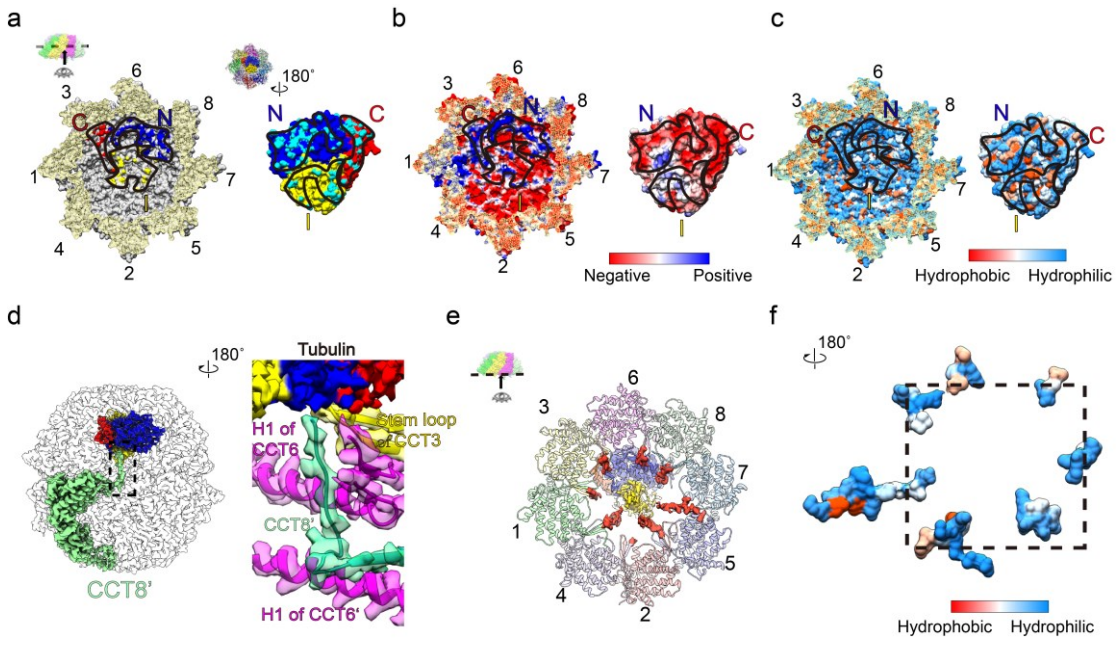

Fig. 4 | Engagement of tubulin with TRiC through electrostatic and hydrophilic interactions, and the roles of TRiC termini in tubulin folding in TRiC-tubulin-S3. **a**, Interaction interface between TRiC and tubulin. The visualization direction and region are shown in the inset. The contact surface residues of TRiC within 4 Å distance of the N/C/I domains of tubulin are colored in blue, red, and yellow, respectively (left panel, black outlines indicate the tubulin footprint on the TRiC interior cavity wall). The contact surface residues of tubulin in proximity to TRiC are colored in cyan (right panel, black outlines indicate the TRiC footprint on the tubulin structure). **b**, An electrostatic surface property analysis, suggesting complementary electrostatic interaction between the CCT3/6/8 subunits of TRiC (mainly positively charged) and the N/C domains of tubulin (mostly negatively charged). **c**, The hydrophilicity/hydrophobicity analysis between TRiC and tubulin, suggesting a hydrophilic interaction between them. **d**, Magnified view of the interaction network of the CCT8' N-terminus. **e**, Depiction showing those resolved portion of C-termini (red density) for all TRiC subunits (besides CCT4) were observed to form contacts with tubulin (central transparent density). **f**, Depiction of the hydrophilicity/hydrophobicity of the resolved C-termini of TRiC, showing these termini to be enriched in hydrophilic residues.

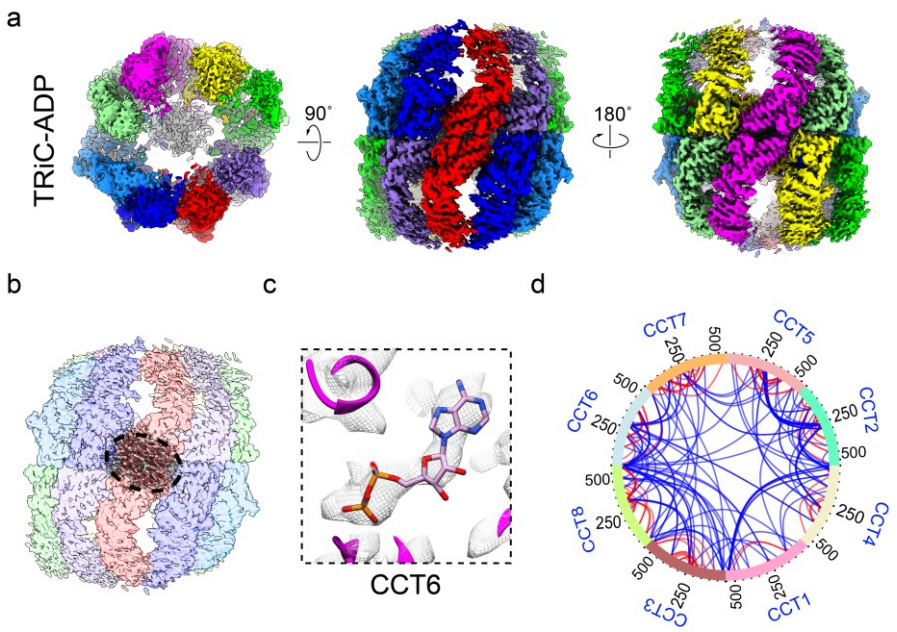

Fig. 5 | Cryo-EM and XL-MS analyses of TRiC in the presence of ADP. **a-b**, Cryo-EM map of TRiC-ADP (**a**), showing the tail density (in grey) remained but substrate released (**b**). **c**, Representative nucleotide density (in the ADP state) of CCT6 in TRiC-ADP. **d**, The XL-MS data showing no cross-links were detected between TRiC and tubulin after ADP incubation. Identified intra-subunit XLs are in red, and inter-subunit XLs in blue.

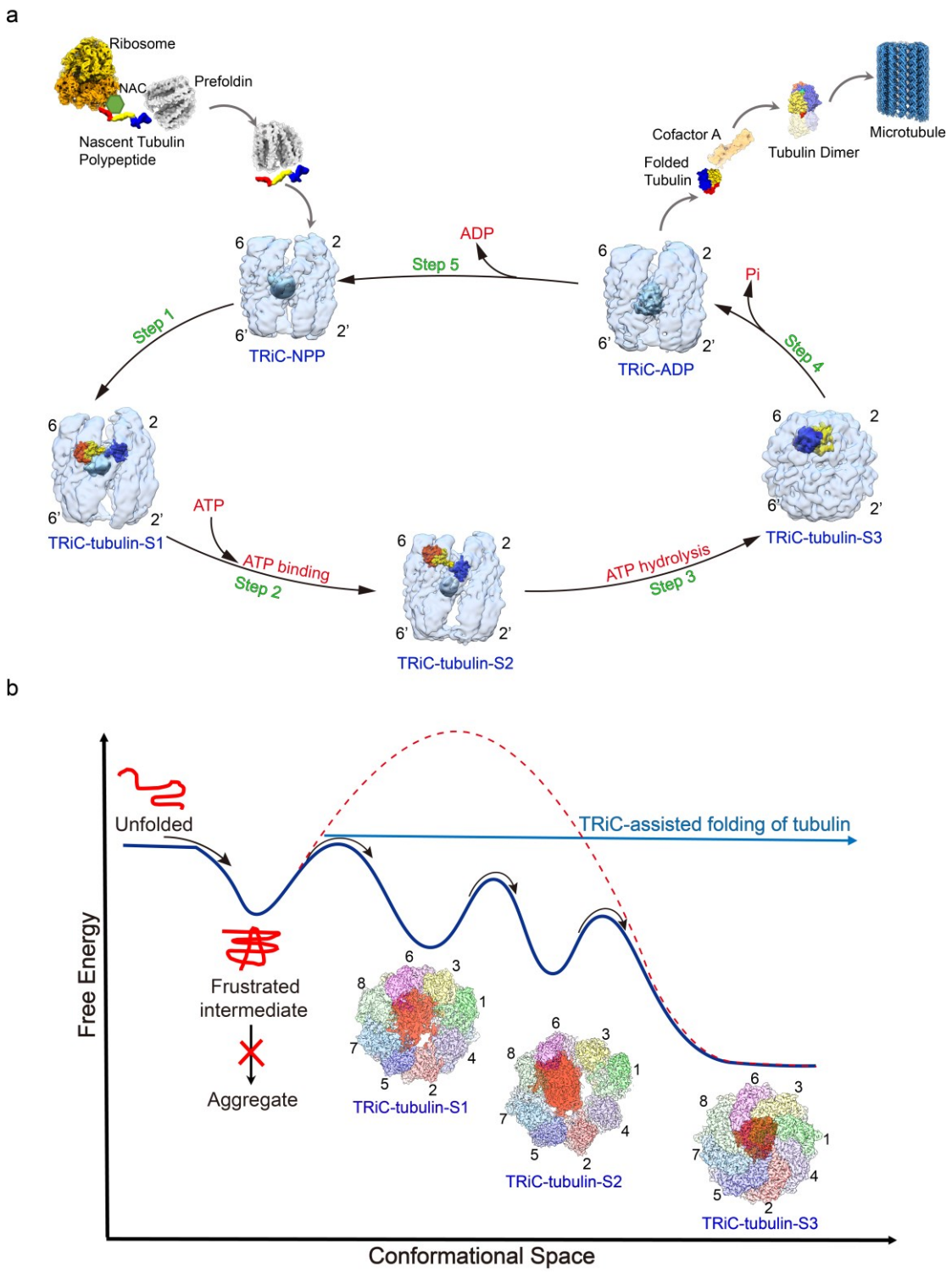

Fig. 6 | The proposed pathway and mechanism of TRiC-mediated tubulin folding. **a**, The proposed pathway of tubulin folding mediated by TRiC associating with its ATP-driven conformational cycle. After being translated from ribosome, nascent tubulin polypeptides are delivered to TRiC-NPP by co-chaperon prefoldin. TRiC is shown in transparent light blue, with its unstructured termini in sky blue density and

CCT2/6 being labeled. Tubulin is then released inside the TRiC chamber, contacting with the E domains of all TRiC subunits and with the unstructured termini of TRiC, to form the TRiC-tubulin-S1 state (step 1). After ATP binding to TRiC, tubulin can gradually translocate upwards to associate with the A/I domains of CCT6/8 in addition to keeping contacts with the E domains, forming the TRiC-tubulin-S2 state (step 2). Once ATP-hydrolysis triggers TRiC ring closure, forming the TRiC-tubulin-S3 state, the generated mechanical force together with the directional contacts and constraints on tubulin could facilitate tubulin folding towards the native state (step 3). Subsequently, in the γ-phosphate released open TRiC-ADP state, the associated tubulin could be released from TRiC chamber (step 4). The dynamic β-tubulin I domain could be capped by cofactor A, then assembled with α-tubulin into tubulin heterodimers. Finally, the tubulin heterodimers assemble into the microtubule. TRiC could then release ADP to resume to the NPP state (step 5). All TRiC maps were low passed to 8 Å for easier visualization. **b**, Hypothetical energy landscape of tubulin folding assisted by TRiC. Without TRiC assistance, nascent tubulin is prone to form aggregates or needs to overcome a high energy barrier to achieve its native state. Engagement of tubulin with TRiC in a manner associated with the TRiC ATPase cycle could potentially confine the energy landscape of tubulin and lower its energy barrier, resulting in stabilization of tubulin and finally becoming folded into a substantially near-native state.

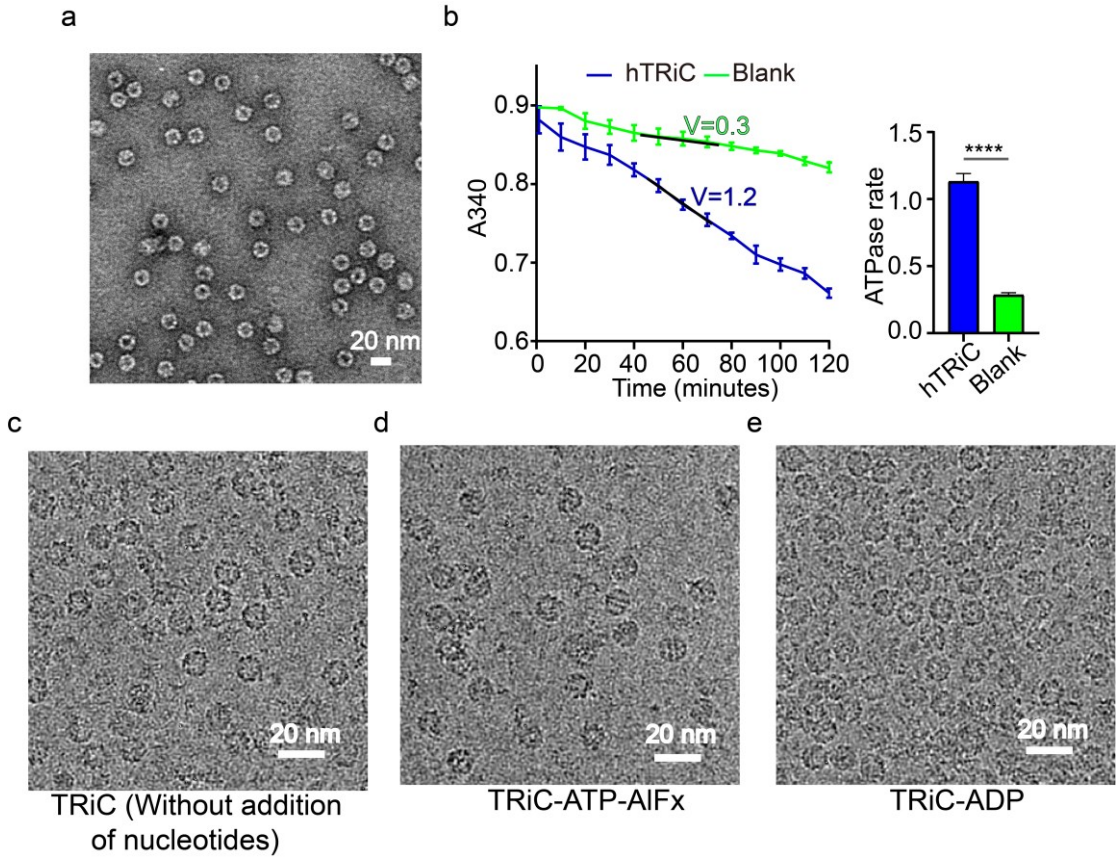

Extended Data Fig. 1 | Human TRiC purified from HEK293F cells. a, Representative negative-stain EM image of purified TRiC. **b**, NADH-coupled enzymatic assays of our purified TRiC and a blank (TRiC buffer without proteins). The results revealed that TRiC was biologically active and could hydrolyze ATP. The ATPase rates (V, with unit of "mole ATP/ [mole TRiC • min]") determined by fitting the linear part of the ATP hydrolysis reaction curves are also provided. An analysis of the significance of the difference between the results (right) suggested that the TRiC sample showed a significantly higher ATPase activity than did the blank, with a statistical significance of ****$P < 0.0001$. For all quantifications, data were plotted as mean ± SD for three independent replicates. **c-e**, Representative cryo-EM images of TRiC sample before adding nucleotides (**c**), in the presence of ATP-AlFx (**d**), and in the presence of ADP (**e**).

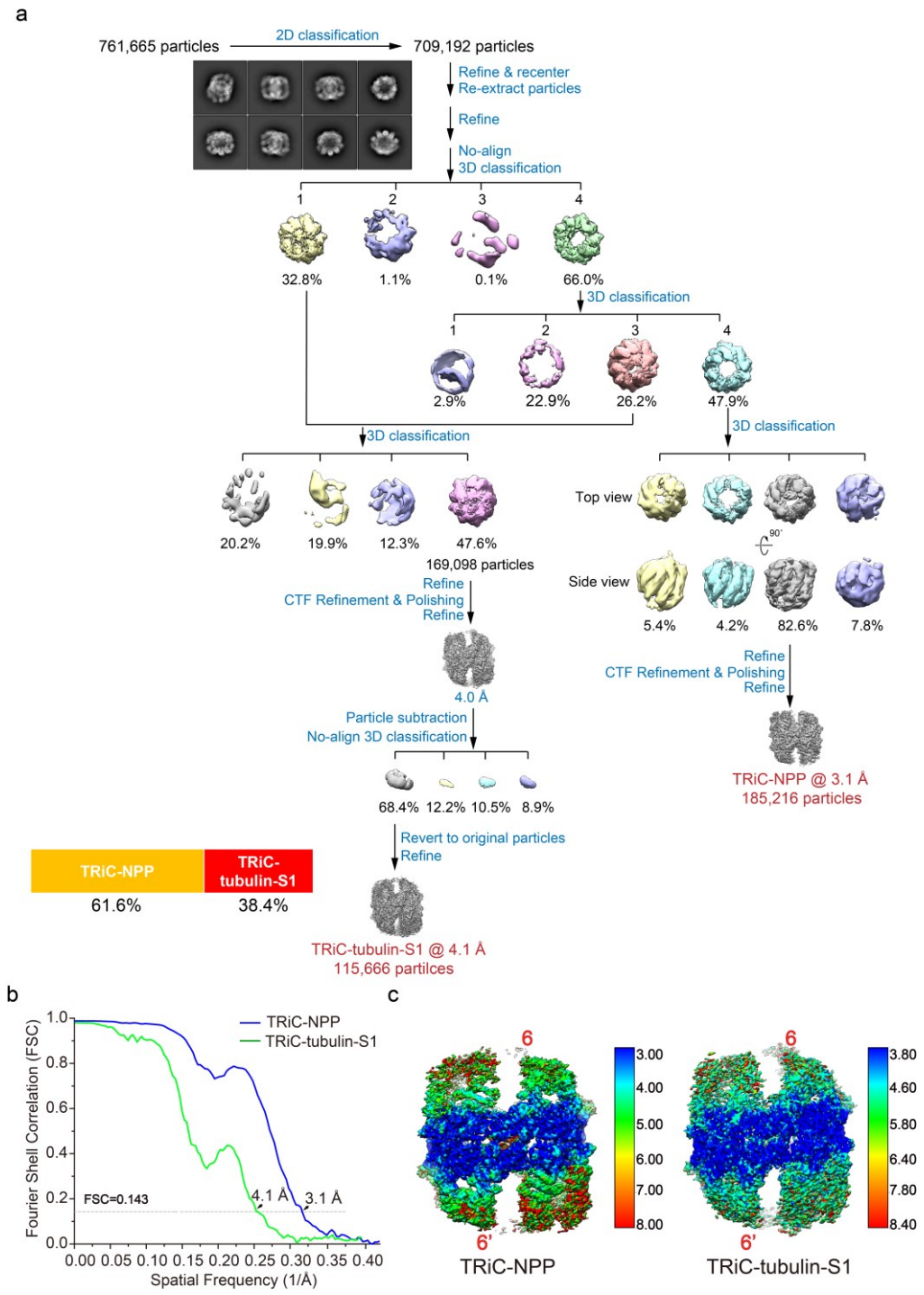

Extended Data Fig. 2 | Work flow for the processing of the cryo-EM data of endogenously purified TRiC. a, Procedure used to process the TRiC cryo-EM data. The reference-free 2D class averages and population distributions of TRiC-NPP and TRiC-tubulin-S1 are also presented. **b-c**, Resolution estimations for TRiC-NPP and TRiC-tubulin-S1 according to the gold-standard FSC criterion of 0.143 (**b**), and local resolution evaluations (**c**).

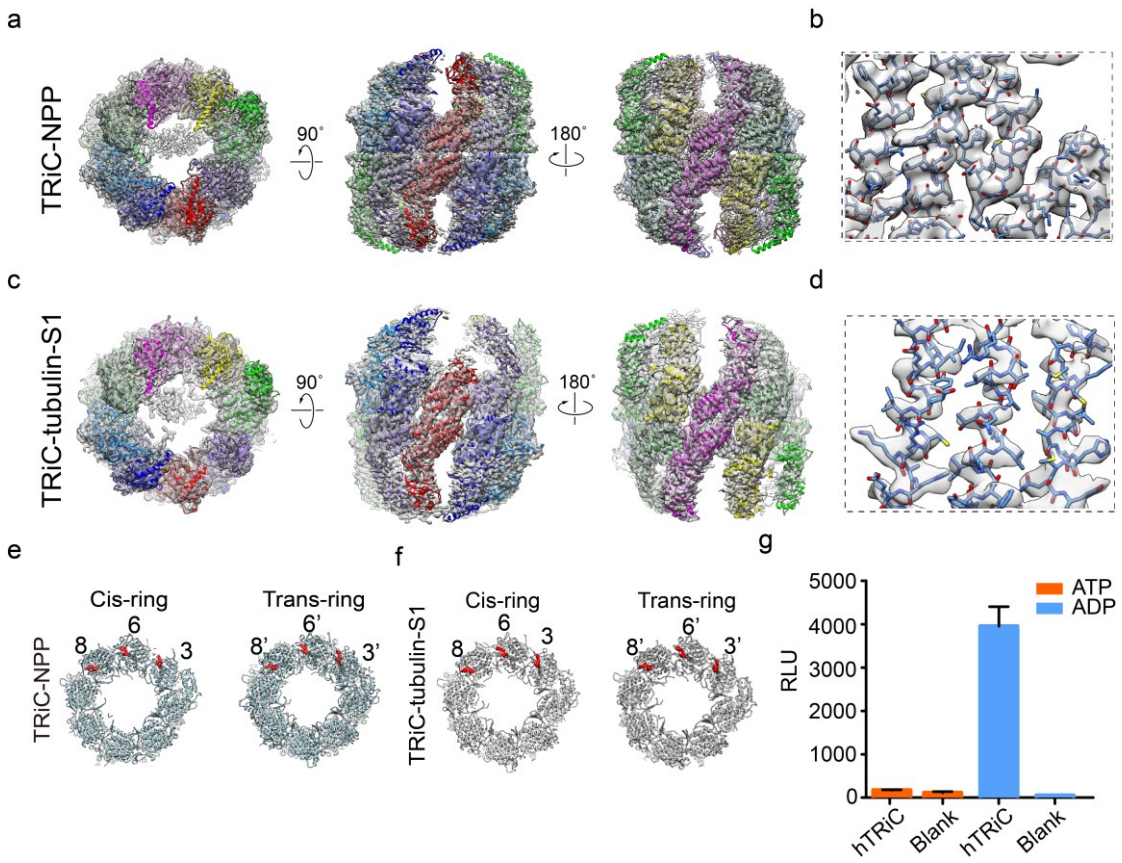

Extended Data Fig. 3 | Atomic models of TRiC-NPP and TRiC-tubulin-S1. **a,c,** Atomic models of TRiC-NPP (**a**) and TRiC-tubulin-S1 (**c**) match well with the corresponding cryo-EM maps. **b,d,** Representative high-resolution structural features of TRiC-NPP (**b**) and TRiC-tubulin-S1 (**d**). **e-f**, Nucleotide occupancy statuses of TRiC-NPP (**e**) and TRiC-tubulin-S1 (**f**), with CCT3/6/8 from both rings having nucleotide density (in red) in their nucleotide pockets. **g**, ATP/ADP ratio analysis of TRiC. The relative light unit (RLU) values were measured for the sample with TRiC buffer as a blank. For all quantifications, data were plotted as mean ± SD for three independent replicates.

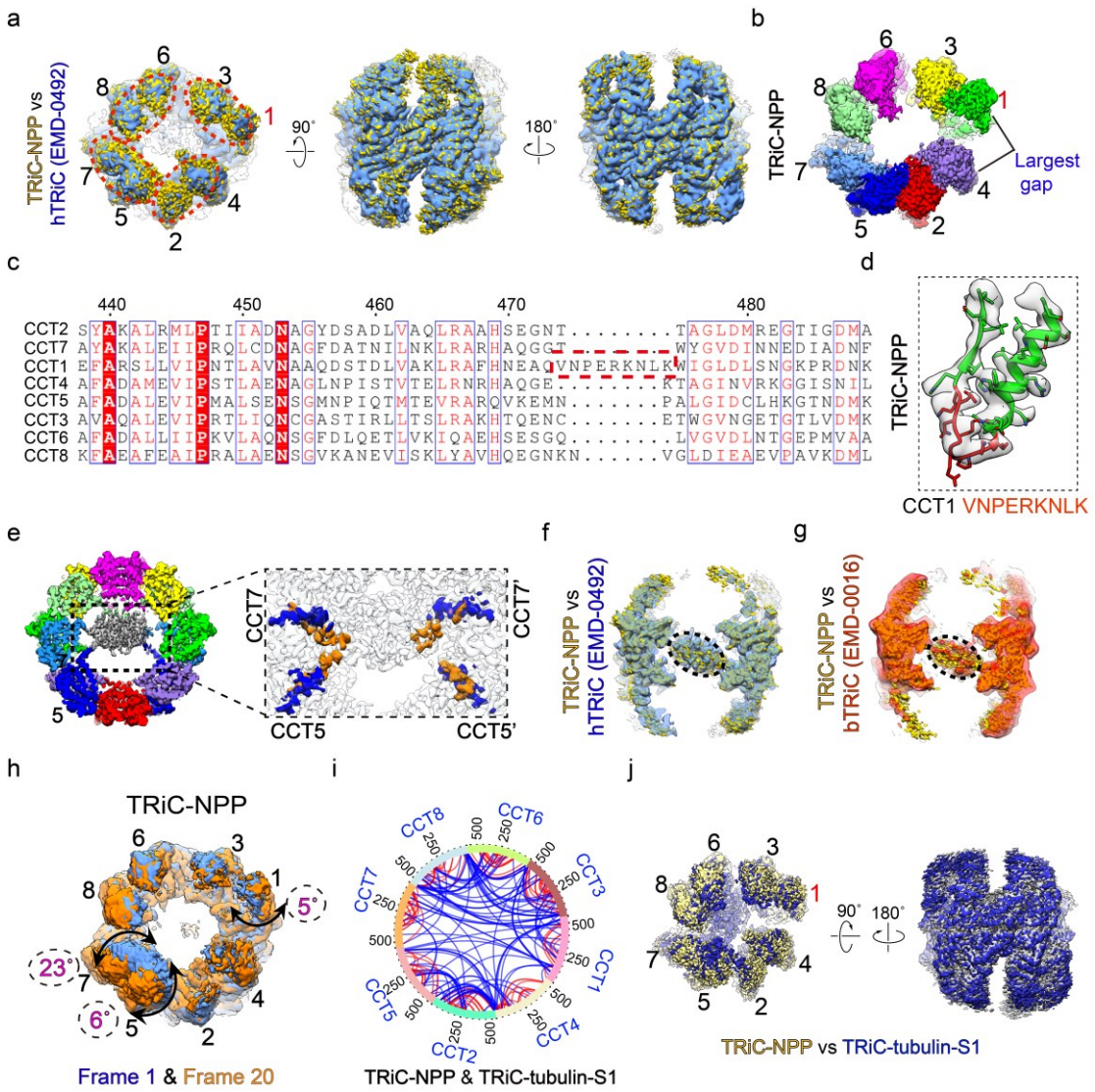

Extended Data Fig. 4 | TRiC-NPP and TRiC-tubulin-S1 conformations and subunit configurations. **a**, Overlay of our TRiC-NPP map (yellow) and the reported apo hTRiC map (cornflower blue, EMDB: 0492), indicating no obvious conformational differences between the two structures. The tetramer-of-dimers pattern is indicated by dotted red circles. **b**, CCT1 and CCT4 display the largest gap between their A domains. **c-d**, Sequence alignment of all the eight subunits of hTRiC, revealing a unique insertion (indicated by red dashed frames) in the E domain of CCT1 (**c**), and the corresponding structural feature of the CCT1 E-domain insertion in TRiC-NPP (**d**). **e**, Depiction of the TRiC-NPP map showing the central tail density symmetrically contacting the N-/C-termini of CCT5/7 and CCT5'/7' from both rings. In the magnified cut-off top view (right), only the resolved N-/C-termini of CCT5/5'

1034 and CCT7/7' are colored, with the C-tails in blue and N-tails in orange. **f-g**, Central
1035 slice view of the TRiC-NPP (yellow) overlaid with apo hTRiC (cornflower blue,
1036 EMDB: 0492[49]) (**f**), and with apo bovine TRiC (red, EMDB: 0016) (**g**), to show their
1037 similar tail density features (indicated by black dashed ellipsoid). **h**, Results for the
1038 3D variability analysis (3DVA) of the TRiC-NPP dataset. This analysis suggested that
1039 CCT7/5/1 underwent a continuous outward/inward tilting motions of up to ~23°/6°/5°,
1040 respectively. Frame 1 (cornflower blue) and frame 20 (orange), together showing the
1041 maximum extent of the conformational change, are displayed. **i**, XL-MS-derived
1042 circular plot of all XLs of the TRiC portion, with intra-subunit XLs shown in red, and
1043 inter-subunit XLs in blue. The detected cross-links within the TRiC complex fulfill
1044 the spatial geometry constrains of the linked amino acids, validating the reliability of
1045 our XL-MS data. **j**, TRiC-NPP map (yellow) overlaid with the TRiC-tubulin-S1 map
1046 (medium blue), indicating no obvious conformational differences between them.

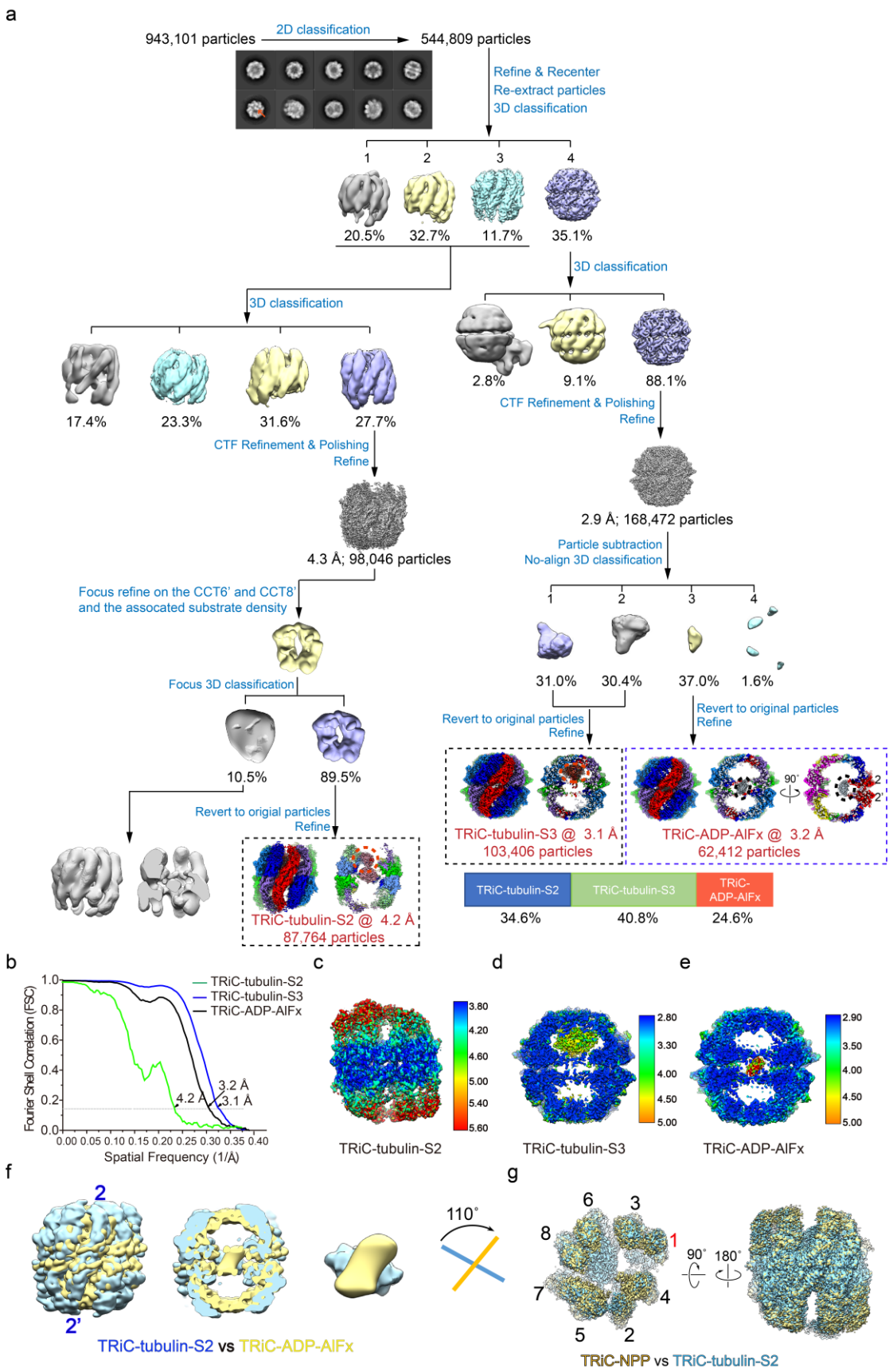

1047

1048 **Extended Data Fig. 5 | Work flow for the processing of the cryo-EM data of**

1049 **TRiC in the presence of ATP-AlFx. a**, Procedure used to process the cryo-EM data
1050 of TRiC in the presence of ATP-AlFx. The reference-free 2D class averages and the
1051 population distributions of the three obtained states are also presented. Besides,
1052 central slice view of the TRiC-ADP-AlFx map revealed the tail density attached to the
1053 CCT2/2' subunit pair. **b**, Resolution estimations of the TRiC-tubulin-S2, -S3, and
1054 TRiC-ADP-AlFx maps according to the gold-standard FSC criterion of 0.143. **c-e**,
1055 Local resolution evaluations for the S2 (**c**), S3 (**d**), and TRiC-ADP-AlFx (**e**) maps. **f**,
1056 Overlay of the TRiC-tubulin-S2 and TRiC-ADP-AlFx maps. When visualized from
1057 the typical viewing direction with the CCT2 subunit pair facing the viewer, the
1058 unstructured tail of TRiC-ADP-AlFx was observed to be rotated clockwise by about
1059 110° relative to that of TRiC-tubulin-S2. These two maps were lowpass filtered to 8 Å
1060 for better visualization of the tail density. **g**, Overlay of the TRiC-NPP (yellow) and -
1061 S2 maps (sky blue), indicating their overall similar conformations.

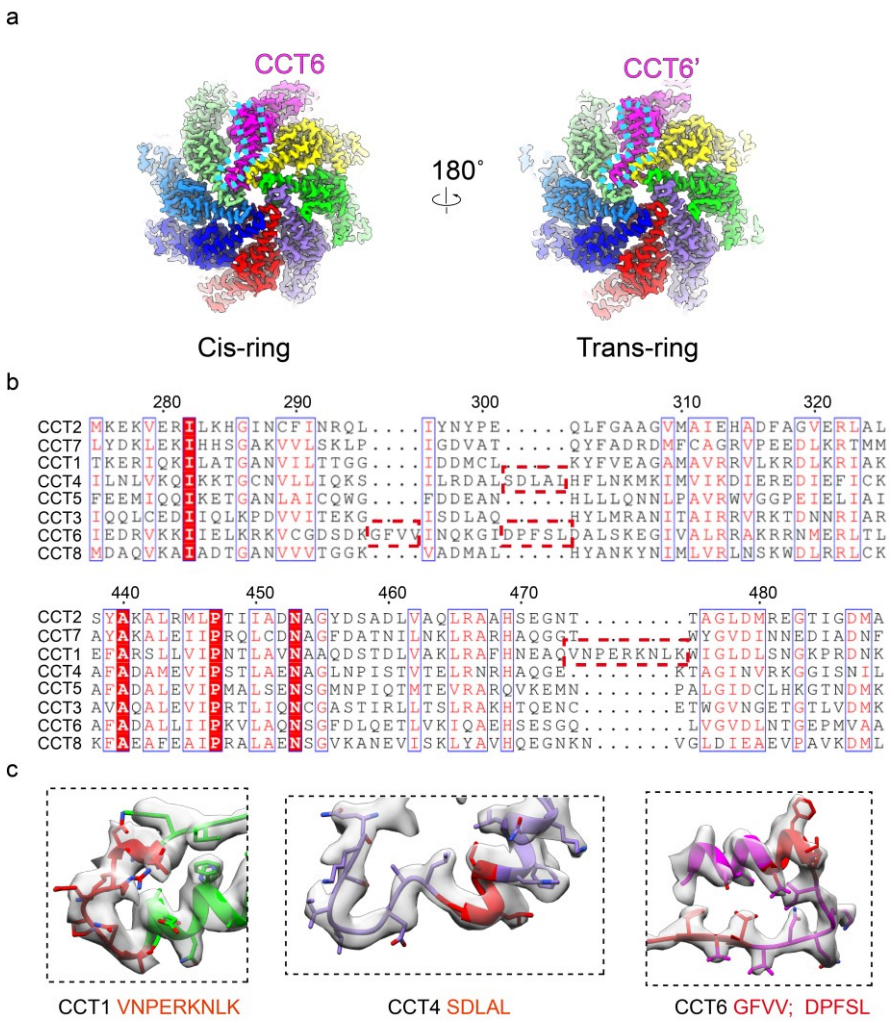

Extended Data Fig. 6 | Features facilitating the subunit identification for the TRiC-tubulin-S3 map. a, Depictions of the S3 map in which the unique kink feature (enclosed in a dotted blue line) in the apical protrusion H8 of CCT6 was unambiguously visualized in both rings, substantiating the on-axis location of CCT6. **b**, Sequence alignment of all eight subunits of hTRiC. This alignment revealed four unique insertions (indicated by red dashed frames) in CCT1/4/6. **c**, Related structures of the four insertions (in red), all resolved in our S3 map.

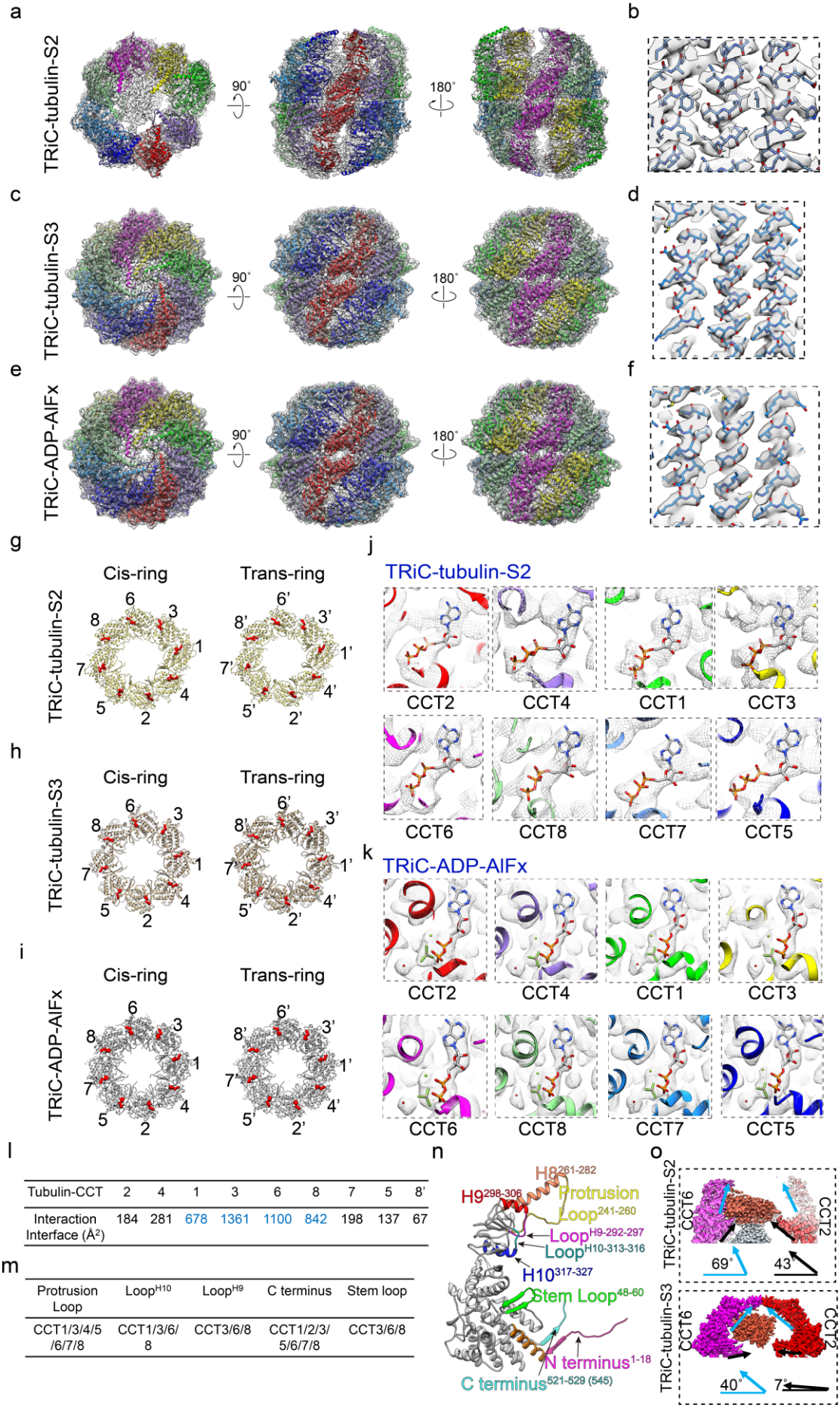

Tubulin-CCT	2	4	1	3	6	8	7	5	8'
Interaction Interface (Å^2)	184	281	678	1361	1100	842	198	137	67

Protrusion Loop	Loop^{H10}	Loop^{H9}	C terminus	Stem loop
CCT1/3/4/5/6/7/8	CCT1/3/6/8	CCT3/6/8	CCT1/2/3/5/6/7/8	CCT3/6/8

1070

1071 **Extended Data Fig. 7 | Atomic models of TRiC-tubulin-S2, -S3, TRiC-ADP-AlFx**
1072 **and nucleotide status in the TRiC-tubulin-S2 and TRiC-ADP-AlFx maps**. **a,c,e**
1073 Atomic models of TRiC-tubulin-S2 (**a**), -S3 (**c**) and TRiC-ADP-AlFx (**e**) match well
1074 with the corresponding cryo-EM maps. **b,d,f**, Representative high-resolution
1075 structural features of TRiC-tubulin-S2 (**b**), -S3 (**d**) and TRiC-ADP-AlFx (**f**). **g-i**,
1076 Nucleotide occupancy statuses of TRiC-tubulin-S2 (**g**), -S3 (**h**) and TRiC-ADP-AlFx
1077 (**i**). **j**, Magnified view of the TRiC-tubulin-S2 nucleotide pocket region of each
1078 subunit. Every subunit appears to include a bound nucleotide density that matches the
1079 ATP model reasonably well, suggesting that the TRiC-tubulin-S2 is in the ATP-bound
1080 state. **k**, Magnified view of the TRiC-ADP-AlFx nucleotide pocket region of each
1081 subunit. Every subunit here was found to be bound with ADP-AlFx (stick model) and
1082 a magnesium ion (green ball), as well as a water molecule (red ball) in an attacking
1083 position, suggesting that each of these subunits is in the ATP-hydrolysis transition
1084 state. **l**, Interaction areas between tubulin and TRiC subunits in TRiC-tubulin-S3 as
1085 calculated using PISA. **m**, Main structural elements of TRiC involved in the
1086 interaction with tubulin in TRiC-tubulin-S3. **n**, Key structural elements of TRiC
1087 involved in the interaction with tubulin, with the residue numbers of these elements
1088 being labeled (CCT3 as a representative subunit). **o**, Depictions of a portion of the S2
1089 and S3 maps (showing CCT6/2 subunits only), suggesting ATP-hydrolysis-induced
1090 TRiC A and E domain downward rotations. In each panel, showing is the angle
1091 between the long axis of the A (in light blue) or E domain (in black) of CCT2 and the
1092 horizontal plane for the corresponding map.

1093

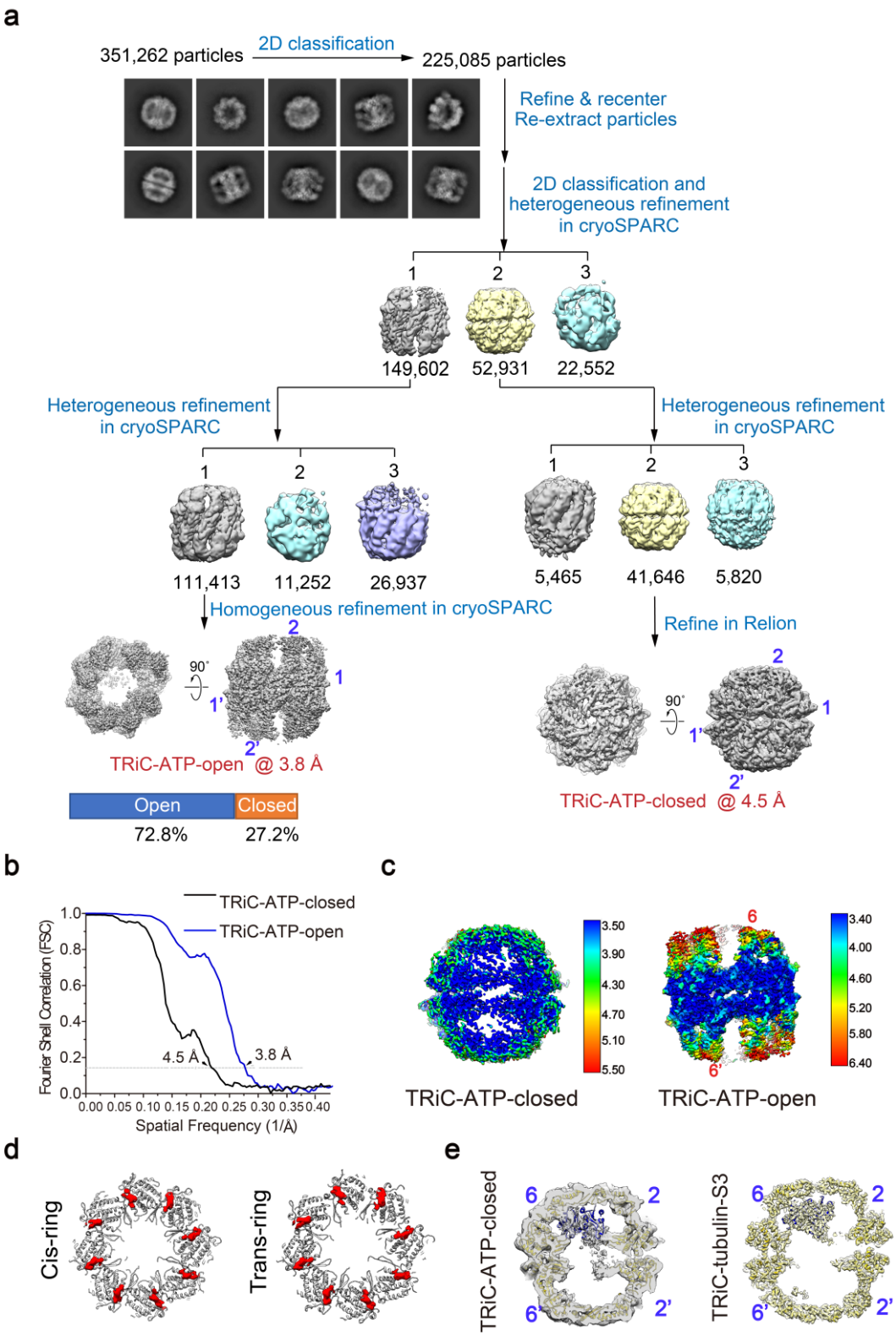

Extended Data Fig. 8 | Cryo-EM analysis of TRiC in the presence of ATP. a, Procedure used to process the cryo-EM data of TRiC in the presence of ATP. Reference-free 2D class averages and population distributions of the closed and open conformations of TRiC (denoted as "TRiC-ATP-closed" and "TRiC-ATP-open",

respectively) are also presented. **b**, Resolution estimations for TRiC-ATP-closed and TRiC-ATP-open maps according to the gold-standard FSC criterion of 0.143. **c**, Local resolution evaluations for TRiC-ATP-closed and TRiC-ATP-open. **d**, The nucleotide occupancy status of TRiC-ATP-closed showed that all nucleotide pockets were occupied. **e**, The central slice of the TRiC-ATP-closed (left, unsharpened map) and TRiC-tubulin-S3 (right) map with fitted model of TRiC-tubulin-S3. This analysis indicates a substrate within one of the TRiC-ATP-closed chambers, in a position and orientation similar to those of tubulin observed in the TRiC-tubulin-S3 map.

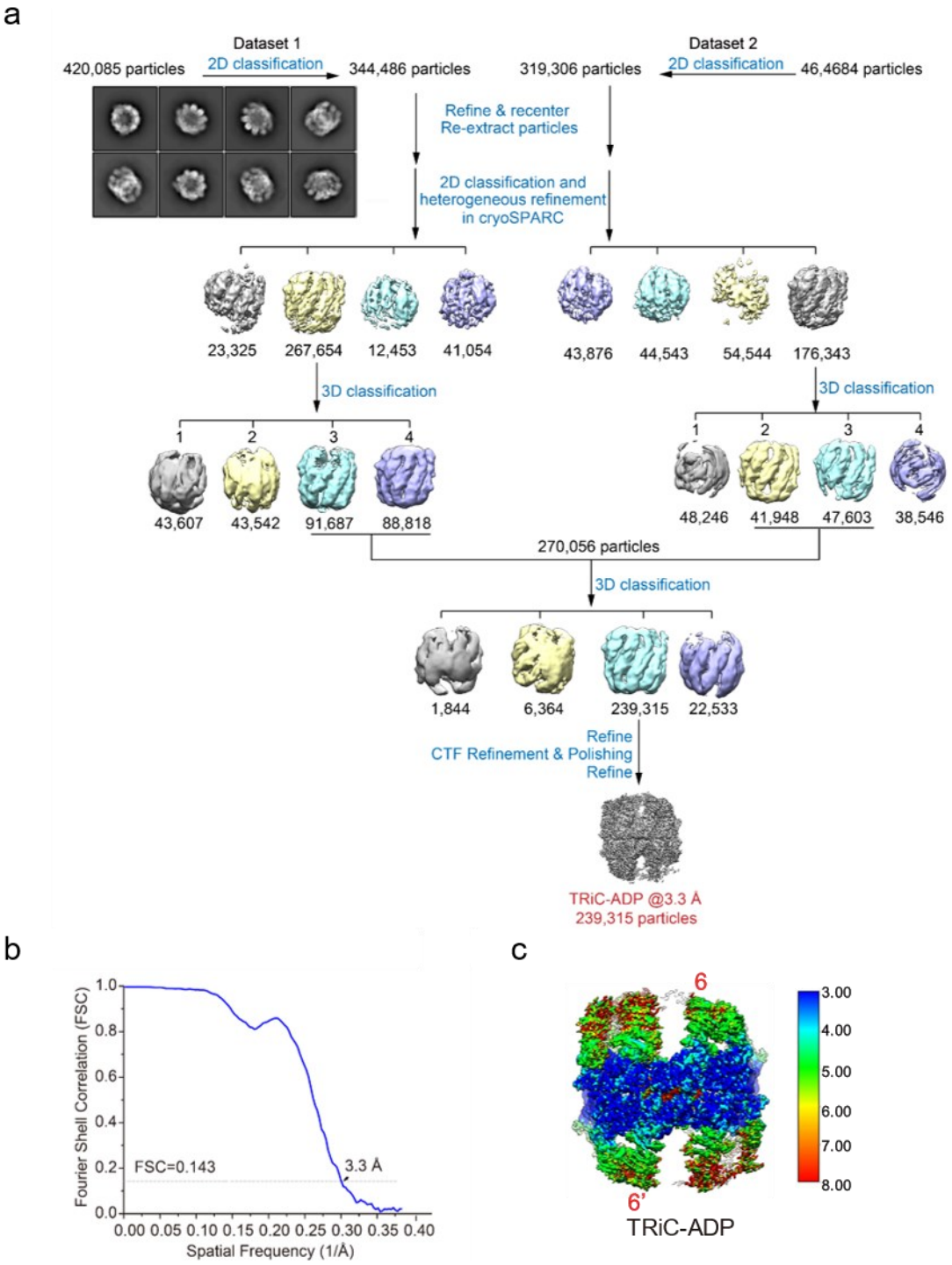

Extended Data Fig. 9 | Work flow for the processing of the TRiC-ADP cryo-EM data. a, Procedure used to process the cryo-EM data of TRiC in the presence of ADP, with the reference-free 2D class average also shown. **b**, Estimation of the TRiC-ADP map resolution according to the gold-standard FSC criterion of 0.143. **c**, Local resolution evaluation for TRiC-ADP.

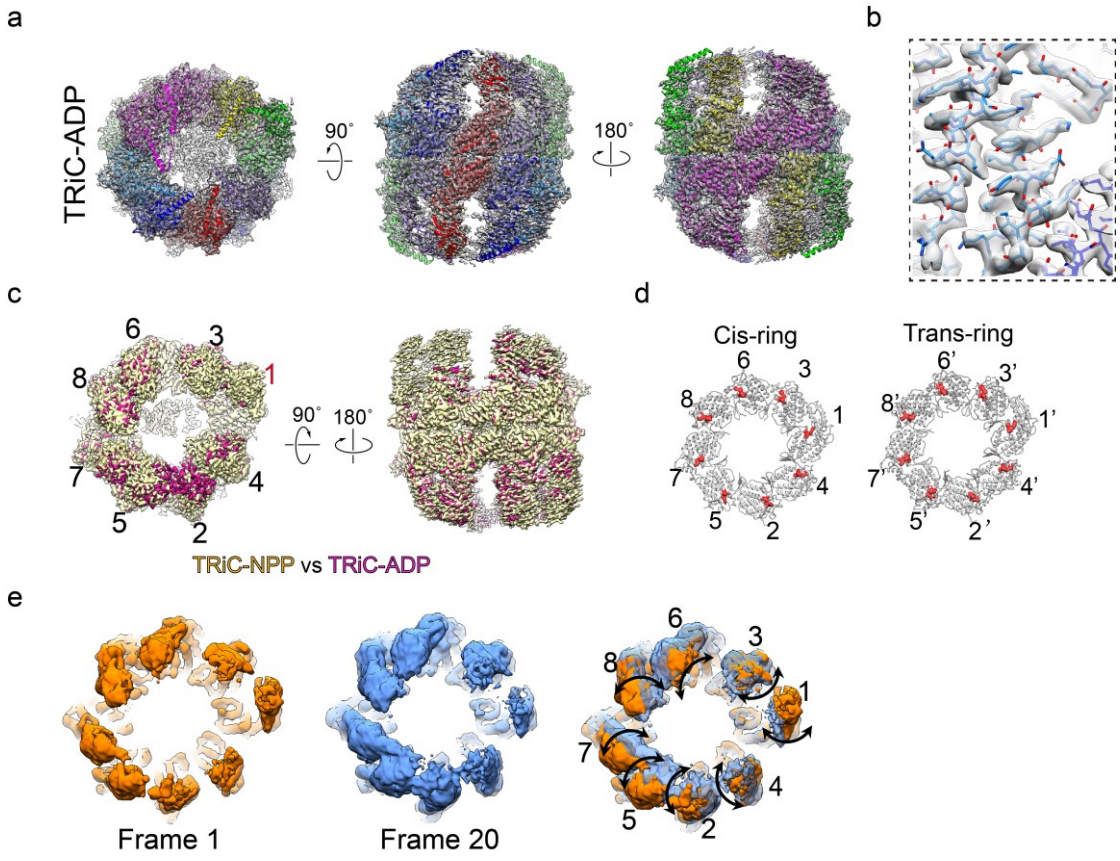

Extended Data Fig. 10 | Atomic model and 3DVA result of TRiC-ADP. a, Atomic model of TRiC-ADP matches well with the corresponding map. **b**, Representative high-resolution structural features of TRiC-ADP. **c**, The determined nucleotide occupancy status of TRiC-ADP, showing all of the subunit nucleotide pockets were occupied. **d**, Overlay of the TRiC-NPP (yellow) and TRiC-ADP (violet red) maps, indicating no large conformational differences between them. **e**, 3DVA results of the TRiC-ADP dataset. This analysis suggested that all of the subunits underwent outward/inward tilting motions. Frames 1 (orange) and 20 (cornflower blue), together showing the maximum extent of the conformational change, are displayed here.

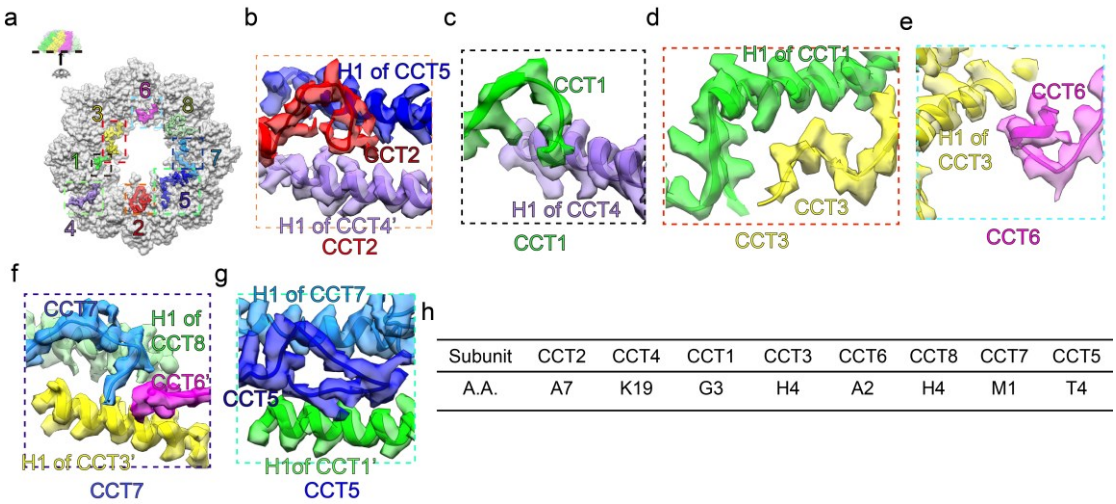

Subunit	CCT2	CCT4	CCT1	CCT3	CCT6	CCT8	CCT7	CCT5
A.A.	A7	K19	G3	H4	A2	H4	M1	T4

Extended Data Fig. 11 | The involvement of the TRiC N-termini in the allosteric interaction network in TRiC-tubulin-S3. a, Locations of the resolved N-termini (in color) in the TRiC-tubulin-S3 structure. The visualization direction and visualized region are illustrated in the inset. **b-g**, Magnified views of the interaction between the N-terminus of CCT2 and helices H1 of CCT5 and CCT4' (**b**), between the N-terminus of CCT1 and H1 of CCT4 (**c**), between the N-terminus of CCT3 and H1 of CCT1 (**d**), between the CCT6 N-terminus (there is a small 1-turn α-helix before its N-terminal β-sheet) and H1 of CCT3 (**e**), between the N-terminus of CCT7 and H1 of CCT8 and CCT3', as well as the N-terminus of CCT6' (**f**), and between the N-terminus of CCT5 and helices H1 of CCT7 and CCT1'(**g**). **h**, The most N-terminal amino acid residue visualized for each subunit of TRiC in the TRiC-tubulin-S3 structure.

1137 **Table 1 | Cryo-EM data collection, processing, and model validation statistics**

	TRiC-NPP (EMDB-32922) (PDB-7X0A)	TRiC-tubulin-S1 (EMDB-32903) (PDB-7WZ3)	TRiC-tubulin-S2 (EMDB-32989) (PDB-7X3J)	TRiC-tubulin-S3 (EMDB-32923) (PDB-7X0S)	TRiC-ADP-AlFx (EMDB-32926) (PDB-7X0V)	TRiC-ADP (EMDB-32993) (PDB-7X3U)	TRiC-ATP-closed (EMDB-33025) (PDB-7X6Q)	TRiC-ATP-open (EMDB-33053) (PDB-7X7Y)
Data collection and processing								
Magnification				18,000			81,000	
Voltage (kV)				300			300	
Detector				K2 summit			K3	
Electron exposure (e–/Å²)				38			50	
Defocus range (μm)				-0.8 to -2.5			-0.8 to -2.5	
Pixel size (Å)				1.318			0.89	
Symmetry imposed				C1			C1	
Initial particle images (no.)	761,665	761,665	943,101	943,101	943,101	884,769	351,262	351,262
Final particle images (no.)	185,216	115,666	87,764	103,406	62,412	239,315	41,646	111,413
Map resolution (Å)	3.1	4.1	4.2	3.1	3.2	3.3	4.5	3.8
FSC threshold				0.143				
Map resolution range (Å)	3.0-8.0	3.8-8.4	3.8-8.4	2.8-4.5	2.9-4.5	3.0-8.0	3.5-5.5	3.4-6.4
Refinement								
Initial model used (PDB code)	5GW4; 5GW5	5GW4; 5GW5	5GW4; 5GW5	6KS6; 5JCO	6KS6	5GW4; 5GW5	6KS6	5GW4; 5GW5
Model resolution (Å)	4.2	7.4	7.2	3.4	3.6	3.6	4.5	4.2
FSC threshold				0.5				
Map sharpening *B* factor (Å²)	-76.7	-133.7	-144.4	-53.3	-80.4	-96.2	-135.8	-111.4
Model composition								
Non-hydrogen atoms	63,694	58,818	63,464	63,367	65,020	63,964	64,486	63,532
Protein residues	8,314	7,686	8,241	8,866	8,440	8,314	8,440	8,314
Ligands	6	6	16	48	48	16		
B factors (Å²)								
Protein	120.55	127.93	31.20	55.75	79.70	33.58	55.28	179.95
Ligand	57.86	45.81	11.53	51.16	72.45	8.06		
R.m.s. deviations								
Bond lengths (Å)	0.005	0.004	0.005	0.003	0.004	0.003	0.091	0.003
Bond angles (°)	0.533	0.996	1.105	0.665	1.072	0.655	1.669	0.886
Validation								
MolProbity score	1.39	1.13	1.40	1.43	1.54	1.17	1.35	1.44
Clashscore	3.67	2.17	4.21	3.19	4.23	1.78	3.45	5.18
Poor rotamers (%)	0.04	0.00	0.07	0.04	0.04	0.07	0.01	0.00
Ramachandran plot								
Favored (%)	96.50	97.25	96.82	95.36	95.10	96.48	96.68	97.09
Allowed (%)	3.47	2.75	3.17	4.64	4.90	3.43	3.16	2.91
Disallowed (%)	0.03	0.00	0.01	0.00	0.00	0.09	0.15	0.00

1138

1139

1140 **Supplementary Table 1 | Results of mass spectroscopy (MS) analysis of**
1141 **endogenously purified TRiC with associated tubulin**

	Protein	Coverage	PSMs	Peptides	Unique peptides
TRiC subunits	CCT1	79	116	39	37
	CCT2	78	199	36	36
	CCT3	73	113	41	41
	CCT4	72	125	33	32
	CCT5	68	139	41	39
	CCT6	64	124	35	30
	CCT7	80	194	39	32
	CCT8	75	121	40	40
TUBB	TUBB5	82	104	47	9
	TUBB4	38	31	16	3
	TUBB2	44	27	14	3
	TUBB6	24	12	7	2
	TUBA4	7	3	3	1
	TUBG1	24	7	6	6
	TUBD1	6	2	2	2

1142

1143 **Supplementary Table 2 | Results of XL-MS analysis of TRiC with associated**

1144 **tubulin**

Protein1 (site) –Protein2 (site) Inter-Protein	Peptides	Score	Spec count
CCT3 (21)-Tubulin (58)	KVQSGNINAAK(1)-ISVYYNEATGGKYVPR(12)	9.35E-09	3
CCT3 (21)-Tubulin (252)	KVQSGNINAAK(1)-KLAVNMVPFPR(1)	7.00E-10	4
CCT4 (21)-Tubulin (58)	GKGAYQDR(2)-ISVYYNEATGGKYVPR(12)	1.42E-22	3
CCT6 (10)-Tubulin (252)	TLNPKAEVAR(5)-KLAVNMVPFPR(1)	8.44E-07	4
CCT8 (16)-Tubulin (252)	APGFAQMLKEGAK(9)-KLAVNMVPFPR(1)	5.15E-06	2

1145

1146 * We used E-value (1.00E-02) and spec count (larger than 1) as the threshold to

1147 remove extra XL-MS data with low confidence.

1148 **Supplementary Table 3 | Results of XL-MS analysis of TRiC with associated**
1149 **tubulin in the presence of ATP-AlFx**

Protein1 (site) –Protein2 (site) Inter-Protein	Peptides	E-value	Spec count
CCT1 (532)-Tubulin (252)	IDDLIKLHPESK(6)-KLAVNMVPFPR(1)	3.12E-04	3
CCT2 (250)-Tubulin (252)	IKIFGSR(2)-KLAVNMVPFPR(1)	5.03E-06	3
CCT2 (522)-Tubulin (252)	VDNIIKAAPR(6)-KLAVNMVPFPR(1)	2.24E-14	9
CCT2 (248)-Tubulin (252)	ILIANTGMDTDKIK(12)-KLAVNMVPFPR(1)	8.77E-05	3
CCT3 (21)-Tubulin (58)	KVQSGNINAAK(1)-ISVYYNEATGGKYVPR(12)	6.03E-08	3
CCT3 (527)-Tubulin (252)	IDDIVSGHKK(9)-KLAVNMVPFPR(1)	1.20E-10	5
CCT3 (21)-Tubulin (252)	KVQSGNINAAK(1)-KLAVNMVPFPR(1)	1.61E-10	4
CCT3 (248)-Tubulin (252)	IVLLDSSLEYKK(11)-KLAVNMVPFPR(1)	5.19E-05	3
CCT4 (2)-Tubulin (252)	PENVAPR(1)-KLAVNMVPFPR(1)	9.06E-11	8
CCT5 (263)-Tubulin (252)	HKLDVTSVEDYK(2)-KLAVNMVPFPR(1)	1.12E-12	4
CCT5 (257)-Tubulin (252)	IAILTCPFEPPKPK(12)-KLAVNMVPFPR(1)	1.55E-05	3
CCT6 (10)-Tubulin (252)	TLNPKAEVAR(5)-KLAVNMVPFPR(1)	2.37E-20	4
CCT7 (55)-Tubulin (252)	GKATISNDGATILK(2)-KLAVNMVPFPR(1)	1.01E-21	4
CCT8 (296)-Tubulin (252)	AIADTGANVVVTGGKVADMALHYANK(15)-KLAVNMVPFPR(1)	2.39E-10	8
CCT8 (225)-Tubulin (58)	KETEGDVTSVK(1)-ISVYYNEATGGKYVPR(12)	4.44E-08	3
CCT8 (225)-Tubulin (252)	KETEGDVTSVK(1)-KLAVNMVPFPR(1)	1.36E-08	2
CCT8 (318)-Tubulin (252)	LNSKWDLR(4)-KLAVNMVPFPR(1)	5.09E-13	5

1150

1151 * We used E-value (1.00E-02) and spec count (larger than 1) as the threshold to
1152 remove extra XL-MS data with low confidence.

Supplementary Table 4 | Interactions between tubulin and CCT3/6/8/1 detected using PISA

	TRiC subunit		Tubulin		Interaction	Distance (Å)
	Residue	Atom	Residue	Atom		
CCT3	GLU 89	[OE1]	LYS 392	[NZ]	Salt bridge/ H bond	3.82
	GLU 69	[OE2]	HIS 396	[NE2]	Salt bridge	3.32
	ARG 313	[NE]	GLU 157	[OE2]	Salt bridge	3.72
	ARG 200	[NH1]	ASP 404	[OD2]	Salt bridge/ H bond	3.65
	ARG 316	[NH1]	GLU 407	[OE2]	Salt bridge/ H bond	3.71
	LYS 317	[NZ]	GLU 410	[OE1]	Salt bridge/ H bond	2.52
	LYS 317	[NZ]	GLU 410	[OE2]	Salt bridge	3.87
	LYS 196	[NZ]	GLU 405	[OE2]	Salt bridge	3.90
	GLU 69	[OE1]	TRP 397	[NE1]	H bond	3.74
	GLU 69	[OE2]	TRP 397	[NE1]	H bond	3.64
	ARG 316	[NH1]	TYR 106	[OH]	H bond	2.48
	ARG 85	[NH1]	ARG 391	[O]	H bond	2.83
	ARG 68	[NH2]	LYS 392	[O]	H bond	3.74
	LYS 203	[NZ]	GLY 400	[O]	H bond	3.30
	ARG 200	[NH1]	MET 403	[O]	H bond	3.33
	ARG 200	[NH2]	MET 403	[O]	H bond	3.49
	ASN 321	[ND2]	MET 406	[SD]	H bond	3.26
	THR 318	[OG1]	GLU 407	[OE2]	H bond	3.03
CCT6	ASP 213	[OD1]	ARG 121	[NH1]	Salt bridge/ H bond	3.22
	ASP 213	[OD1]	ARG 121	[NH2]	Salt bridge	3.41
	ASP 213	[OD2]	LYS 122	[NZ]	Salt bridge/ H bond	2.45
	ARG 319	[NH1]	ASP 114	[OD2]	Salt bridge	3.49
	ARG 319	[NH2]	ASP 114	[OD2]	Salt bridge/ H bond	2.73
	ARG 314	[NH2]	ASP 128	[OD1]	Salt bridge/ H bond	3.17
	ARG 318	[NH1]	GLU 157	[OE1]	Salt bridge/ H bond	3.27
	GLU 357	[OE1]	THR 55	[OG1]	H bond	2.84
	ARG 315	[O]	ARG 121	[NH1]	H bond	3.28
	ASP 213	[OD2]	ARG 121	[NH2]	H bond	2.44
	TYR 239	[O]	ARG 162	[NH1]	H bond	3.48
	ALA 51	[N]	ASP 74	[OD2]	H bond	3.58
	ARG 314	[NH2]	GLU 125	[O]	H bond	2.48
	ARG 314	[NH1]	ASP 128	[O]	H bond	3.89
	ARG 217	[NE]	GLU 125	[O]	H bond	3.04
	GLY 215	[N]	GLU 125	[OE2]	H bond	3.79
	GLU 238	[OE1]	LEU 130	[N]	H bond	3.75
	GLN 294	[NE2]	GLU 158	[OE1]	H bond	2.69
CCT8	GLU 252	[OE1]	ARG 2	[NE]	Salt bridge/ H bond	3.27
	GLU 252	[OE1]	ARG 2	[NH2]	Salt bridge/ H bond	3.26
	ARG 314	[NE]	ASP 41	[OD2]	Salt bridge	3.69
	ARG 314	[NH1]	ASP 41	[OD1]	Salt bridge	3.51
	LYS 318	[NZ]	ASP 128	[OD2]	Salt bridge/ H bond	3.58
	GLU 252	[O]	ARG 2	[NH2]	H bond	2.98
	LYS 225	[NZ]	TYR 36	[OH]	H bond	3.67
	ARG 314	[NH1]	ASP 41	[OD2]	H bond	2.97
	ASN 316	[ND2]	ASP 41	[OD1]	H bond	2.68
	SER 317	[OG]	GLU 53	[OE2]	H bond	2.34
	LYS 318	[N]	GLU 53	[OE1]	H bond	3.28
	TRP 319	[NE1]	GLU 53	[O]	H bond	2.66
CCT1	ARG 309	[NH2]	GLU 410	[OE1]	Salt bridge/ H bond	3.66
	ASP 358	[O]	LYS 392	[NZ]	H bond	2.94
	GLN 242	[NE2]	ASP 417	[OD1]	H bond	3.81
	GLN 242	[OE1]	GLN 424	[NE2]	H bond	3.55
	ARG 310	[NH2]	ASN 416	[O]	H bond	3.31
	ARG 310	[NH2]	SER 420	[OG]	H bond	2.74

Supplementary Video Legends

Supplementary Video 1 | 3D variability analysis (3DVA) of the TRiC-NPP cryo-EM data. The 3DVA results suggested that the A/I domains of CCT1/4/2/5/7 subunits are overall relative dynamic, with those of CCT7/5/1 even displaying larger movements.

Supplementary Video 2 | 3D variability analysis (3DVA) of the TRiC-ADP cryo-EM data. The 3DVA results suggested that TRiC-ADP was very dynamic with all of the subunits, including the usually most stable CCT6 subunit, displaying an outward/inward tilting motion.